# Spatially resolved translational dysregulation in *Grin2a*+/- mouse model of schizophrenia

Mingrui Wu[1,2], Jiahao Huang[1,2], Sameer Aryal[1,4], Zohreh Farsi[1,4], Hongyu Chen[1,2], Yiming Zhou[1], Shuchen Luo[1,2], Wendy Xueyi Wang[1,2], Kevin Bonanno[1,5], Margaret Yin[1,4], Inès Picard[1,4], Borislav Dejanovic[1,4], Hasmik Keshishian[1,5], Steven A. Carr[1,5], Morgan Sheng[1,3,4], Xiao Wang[1,2,4]

[1]Broad Institute of MIT and Harvard, Cambridge, MA, USA.

[2]Department of Chemistry, Massachusetts Institute of Technology, Cambridge, MA, USA.

[3]Department of Brain and Cognitive Sciences, Massachusetts Institute of Technology, Cambridge, MA, USA.

[4]Stanley Center for Psychiatric Research, Broad Institute of MIT and Harvard, Cambridge, MA, USA.

[5]The Proteomics Platform, Broad Institute of MIT and Harvard, Cambridge, MA, USA.

## Abstract

Loss-of-function (LoF) mutations of *GRIN2A*, encoding the GluN2A subunit of N-methyl-D-aspartate receptor (NMDAR), confer a high risk for schizophrenia (SCZ)[1–3], yet how they affect diverse brain cell types remains poorly understood. Here, we combined subcellular-resolution spatial omics technologies, STARmap[4] and RIBOmap[5], to jointly resolve single-cell transcriptomes and translatomes for 3,447 genes in the brains of *Grin2a*+/- mice and their wild-type littermates across 538,188 cells. Translational dysregulation was markedly more prominent than transcriptional changes in neurons. Across neuronal subtypes, a set of genes including *Camk2a*, *Arc*, *Egr1*, *Egr3*, *Chmp2b*, and *Pja2* exhibited translational reduction in a *Grin2a* gene dose-dependent fashion, suggesting a connection between NMDAR hypofunction and reduced protein synthesis of downstream synaptic plasticity effectors. In interneurons (particularly parvalbumin interneurons), a strong reduction of *Gad2* translation implies loss of inhibitory function in cortical microcircuits, which has long been hypothesized for SCZ pathophysiology. Non-neuronal cell types including astrocytes, oligodendrocytes, and vascular cells also exhibited region-specific translational changes in neurotransmitter transport, lipid synthesis, myelination, and stress response pathways, some of which co-varied with regional neuron state. Together, our study reveals brain-wide translation dysregulation as a critical mechanism underlying SCZ pathophysiology.

## Introduction

Schizophrenia (SCZ) is a chronic and severe neuropsychiatric disorder affecting approximately 1% of the global population[6,7]. It is characterized by a constellation of symptoms, including delusions, hallucinations, cognitive impairments, and social withdrawal[1,8]. Despite decades of research, the molecular and neurobiological basis for SCZ remains poorly understood, while current pharmacological treatments, primarily targeting the dopaminergic signaling pathway, offer only partial relief to symptoms and are ineffective for many patients[1].

SCZ has a strong genetic basis (heritability 60-80%)[9–11], with h undreds of associated common variants of small effect identified through genome-wide association study (GWAS)[2,12]. Recent exome sequencing study from the Schizophrenia Exome Sequencing Meta-analysis (SCHEMA) consortium further revealed risk genes with rare loss-of-function (LoF) variants that confer substantial risk for SCZ[3,13]. Many of these SCZ risk genes converge on pathways related to synapse formation, structure, and function, with particular enrichment in glutamatergic neurotransmission[13].

*GRIN2A*, encoding the GluN2A subunit of the N-methyl-D-aspartate receptor (NMDAR)[14], has been repeatedly identified as a risk gene for SCZ in large-scale common[2] and rare variant[3] human genetics studies. This association between *GRIN2A* LoF and SCZ is in line with the hypoglutamatergic hypothesis of SCZ, which posits that dysfunction of glutamatergic neurotransmission contributes to SCZ pathophysiology[15–17]. Notably, *Grin2a* heterozygous mutant mice show EEG abnormalities and other neurobiological features that resemble those observed in humans with SCZ[18,19]. Transcriptomic characterization of *Grin2a*+/- mice revealed widespread alterations in activity-, mRNA translation-, and metabolism-related genes across different brain regions[19]. However, transcriptome profiling alone cannot inform whether observed changes in mRNA reflect alterations in protein abundance—a critical gap given that mRNA levels correlate poorly with protein expression and that translational dysregulation has emerged as a key mechanism in neurodevelopmental and psychiatric disorders[20–24]. Direct measurement of actively translated mRNAs is therefore essential to determine the extent to which *Grin2a*+/- contributes to SCZ pathophysiology via translational alterations.

To address this question, we employed both STARmap and RIBOmap to create an integrative spatial map of molecular changes in the *Grin2a*+/- mouse brain with micron-level spatial precision. STARmap enables spatially resolved quantitation of mRNA transcripts *in situ*, while RIBOmap extends this capability by selectively measuring ribosome-associated mRNAs, thereby dissecting transcriptional versus translational alterations. By integrating these data layers, we clarify the cell-type- and region-specific effects of *Grin2a* LoF, providing unprecedented insights into the cellular and circuit pathophysiology underlying the *Grin2a*+/- model of SCZ.

## Results

### Spatial transcriptional and translational co-profiling of *Grin2a*+/- mouse brain

We applied STARmap and RIBOmap to profile 3,447 genes of interest in brains from *Grin2a*+/- mice and their wild-type littermates at 12 weeks of age (**Fig. 1a, Supplementary Table 1**). The 3,447-gene panel was compiled from a pool of canonical brain cell-type markers, along with genes shown to be differentially expressed in bulk RNA-seq, single-nucleus RNA-seq (snRNA-seq), or proteomic profiling of *Grin2a* mutant mice[19,25]. We sampled the brain at three coronal positions along the anterior-posterior axis and, at each position, collected two adjacent 20-μm slices to be processed with STARmap and RIBOmap, respectively (**Fig. 1a**). In total, we profiled 24 brain slices, which together included 538,188 cells (**Extended Data Fig. 1a,b**) and covered multiple brain regions implicated in SCZ[26–28], such as prefrontal cortex (PFC), somatosensory cortex (SSC), striatum (ST), hippocampus (HP), and thalamus (TH).

To generate cell-type annotations for downstream analysis, we first integrated the single-cell transcriptomic and translatomic profiles with 1,017 canonical cell type markers (**Extended Data Fig. 1c,d**) and identified 16 major cell types and 30 subpopulations through unsupervised Leiden clustering (**Fig. 1b,c**). Clusters were annotated according to the spatial mouse CNS atlas by Shi *et al*[25]. In detail, we resolved 7 major neuronal cell types, including telencephalon excitatory neuron (TEGLU), diencephalon excitatory neuron (DEGLU), telencephalon inhibitory neuron (TEINH), and medium spiny neuron (MSN), and 9 major non-neuronal cell types, including astrocyte (AC), oligodendrocyte (OLG), microglia (MGL), and pericyte (PER) (**Extended Data Fig. 2a, 3a**). Their respective subclusters correspond to distinct spatial localization patterns (**Fig. 1c**) and functional roles. For example, TEGLU subtypes separated spatially into cortical layers and the Cornu Ammonis (CA) in the hippocampus, while two MSN subclusters, both localized in the striatum, respectively represent direct-pathway and indirect-pathway spiny projection neurons (dSPNs and iSPNs) (**Extended Data Fig. 2b**).

To assess spatial heterogeneity across and within brain regions, we identified 23 molecular tissue regions using SPIN[29] (**Fig. 1d,e, Extended Data Fig. 3b,c**), including cortical layers (CTX_L2/3, CTX_L4, CTX_L5, CTX_L6), PFC regions (CTX_ILA2/3, CTX_mPFC5), hippocampal fields (CTX_CA1, CTX_CA3, CTX_DG, CTX_HIP), and thalamic compartments (TH_1, TH_2, TH_EPI, TH_RT). Notably, the resolution of our method was sufficient to delineate fine tissue structures. For instance, the thalamic reticular nucleus (TRN) emerged as a discrete domain from TH_1 and TH_2 (**Fig. 1e**). The TRN (TH_RT) is challenging to isolate by anatomical dissection, yet is crucial for regulating thalamocortical signaling and a key node implicated in SCZ pathophysiology[30,31]. Cell-type enrichment across molecular tissue regions was concordant with current neurobiological understandings. For example, MSN and DEGLU were predominantly enriched in the striatum (STR) and the thalamus (TH_1, TH_2), respectively (**Fig. 1c , Extended Data Fig. 3d**). Together, these labels provide a basis for identifying disease-associated changes that localize to specific cell types and brain regions.

## RIBOmap reveals global translational reduction of synapse- and translation-associated gene modules

To gain an overview of transcriptional and translational changes in *Grin2a*+/- animals, we applied consensus non-negative matrix factorization (cNMF)[32] to identify gene modules with distinct expression patterns across the entire dataset (**Fig. 2a, Extended Data Fig. 4a,b**). Among the 35 modules identified, 24 showed cell-type-specific enrichment (M1-M24), while 11 were not confined to particular cell types (M25-M35) (**Extended Data Fig. 4c,d, Supplementary Table 2**). Differential expression analysis of cNMF modules revealed greater downregulation in RIBOmap compared to STARmap, particularly for M2, M4, M7, M27, M28, M29, and M33, indicating potential reduction at the translational level for these modules in *Grin2a*+/- animals (**Fig. 2a, bottom two rows**). We also noticed a higher number of differentially expressed genes (DEGs) detected by RIBOmap than by STARmap for most major cell types, further highlighting dysregulation of translational states not obvious at the mRNA level (**Fig. 2a right**). To identify the biological processes associated with each cNMF module, we performed Gene Ontology (GO) enrichment analysis on the top 50 genes within each module[33] (**Fig. 2b**). As anticipated, cell-type-specific modules were enriched for canonical functions of their respective cell types, such as glutamatergic synaptic transmission (M1) in TEGLU, neuropeptide activity (M5) in TEINH, microglia cell activation and synapse pruning (M17) in MGL; while non-cell-type-specific modules showed broader functional enrichments such as postsynaptic density (M28) and translation (M33).

To identify cNMF modules that explain the most difference between WT and *Grin2a*+/- mutant, we trained a Random Forest classifier to predict genotype labels within major cell types and ranked modules based on their feature importance (**Fig. 2c**). Notably, M28 and M29 were key genotype-associated features of TEGLU, TEINH, MSN, and DEGLU populations in RIBOmap, while M31-33 effectively classified TEGLU in STARmap. Additionally, M35 emerged as a top genotype-associated feature for vascular populations (PER, VEN, VLM) across both datasets. We next aimed to gain neurobiological insights from region-specific changes of these genotype-associated modules. Two broad observations emerged (**Fig. 2d**): First, module-level gene expression changes demonstrated spatial heterogeneity not only among major brain structures but also within subregions, highlighting the detailed regulatory signatures that bulk methods overlook. Second, modules displayed distinct patterns at the transcriptomic and translatomic levels. In detail, synaptic function-related modules (M28, M29) were generally downregulated at the translational level (RIBOmap) across most regions, but upregulated at the mRNA level (STARmap) in areas including CTX_L4, CTXsp, CTX_ILA2/3, and STR. Additionally, translation-related module M33 showed downregulation in prefrontal cortex (CTX_mPFC5) and slight upregulation in other cortical layers, striatum, and hippocampus in STARmap, consistent with previous snRNA-seq findings in *Grin2a* LoF mutants[19]. In contrast, M33 was downregulated across the entire cortex in RIBOmap, particularly in CTX_L5, CTX_mPFC5, and fiber tracts (FT). Such a discrepancy between STARmap and RIBOmap is indicative of translational regulation, as supported by global downregulation of the translation-related module M33, which might result in

147 a net reduction in protein synthesis despite rising mRNA levels. This integrative analysis of gene
148 modules showed that neuronal populations and many gene modules, particularly those
149 associated with synaptic functions, exhibited greater translational than transcriptional alterations.

150 ***Grin2a* LoF triggers distinct molecular responses in major neuronal populations**

151 To dissect single-gene alterations upon *Grin2a* LoF in neurons, we first examined the primary
152 excitatory and inhibitory neuronal cell types in our dataset: TEGLU, DEGLU, TEINH, and MSN
153 (**Fig. 3a-e**). These four cell types exhibited relatively high *Grin2a* expression (**Extended Data Fig.**
154 **5a**) and showed extensive molecular changes at both transcriptional and translational levels.

155 The prominent impact on TEGLU and DEGLU is consistent with the primary role of NMDAR in
156 excitatory glutamatergic neurotransmission: GluN2A-containing NMDARs are predominantly
157 localized to excitatory synapse, where they mediate calcium-dependent signaling and synaptic
158 plasticity essential for learning and memory[34,35]. Despite shared disruption of synaptic plasticity
159 genes (*Camk2a*, *Ppp3ca, Arc*), TEGLU and DEGLU exhibited markedly different profiles of
160 glutamatergic pathway alterations, with TEGLU showing substantially more extensive
161 dysregulation (**Fig. 3a,b,f**). In cortical TEGLU, the impact of *Grin2a* haploinsufficiency was much
162 stronger in RIBOmap (translatome) than in STARmap (transcriptome). *Grin2a*+/- was associated
163 with concurrent RIBOmap downregulation of *Grin1*, encoding the obligatory NMDA receptor
164 subunit, and *Grin2b*, encoding the alternative GluN2B subunit, suggesting a general lessening of
165 NMDA receptor-mediated signaling rather than compensatory subunit switching. Moreover,
166 translational downregulation extended to AMPA receptor subunits (*Gria2*, *Gria3*), metabotropic
167 glutamate receptors (*Grm5*, *Grm3*), and vesicular glutamate transporter *Slc17a7* (**Fig. 3a,f,**
168 **Supplementary Table 3**). We also found widespread downregulation of glutamatergic
169 postsynaptic scaffolds (*Dlg1*, *Dlg2*, *Dlgap3*, *Shank2*) and synaptic adhesion molecules (*Nrxn1*,
170 *Nrxn2*) by RIBOmap. Downstream signaling components (*Camk2b*, *Camk2g*, *Homer1*) and some
171 activity-regulated genes (*Egr1*, *Egr3*, *Nrn1*, *Arc, Nptxr*) were also reduced in RIBOmap (**Fig. 3f,**
172 **Supplementary Table 3**). These changes collectively indicate failure of glutamatergic
173 neurotransmission and attenuated synaptic plasticity in cortical excitatory neurons, which may
174 contribute to SCZ-associated cognitive deficits. Compared with cortical TEGLU neurons, thalamic
175 DEGLU exhibited fewer translatomic changes, with downregulation affecting genes involved in
176 calcium-dependent signaling (*Camk2a*, *Ppp3ca*, *Pcp4*), while activity-regulated genes were
177 relatively unperturbed (**Fig. 3b,f**).

178 Excitatory-inhibitory (E/I) balance is critical for proper cortical circuit function and cognition, and
179 its disturbance has been repeatedly implicated in SCZ pathophysiology[36–38]. Studies of
180 postmortem brain tissue from SCZ patients have revealed reduced expression of various
181 GABAergic markers, including GAD1 (also known as GAD67) and parvalbumin (PV), particularly
182 in cortical interneurons[39,40]. Such findings have led to the idea that dysfunction of cortical
183 microcircuits involving both inhibitory interneurons and excitatory pyramidal neurons underlies the
184 cognitive deficits of SCZ. In our spatial RIBOmap analysis, all four TEINH subtypes: TEINH_1-

185 [*Pvalb_Gad1*], TEINH_2-[*Sst_Npy*], TEINH_3-[*Lamp5_Npy*], and TEINH_4-[*Vip_Cnr1*], showed
186 marked reduction in translation of *Gad2*, with the largest magnitude of effect (|Log2FC| > 2) in PV
187 interneurons (TEINH_1-[*Pvalb_Gad1*]) (**Fig. 3c, Extended Fig. 6b**). As GAD2 is concentrated in
188 GABAergic terminals and its level is regulated by activity[41], the suppression of *Gad2* translation
189 suggests reduced activity-dependent GABA release at presynaptic terminals of these inhibitory
190 interneurons. Impairment of PV interneuron function could explain the abnormal gamma
191 oscillations observed in *Grin2a*+/- mice[19] and in human SCZ[42]. Among all brain regions, the
192 inhibitory neurons of the TRN, involved in control of attention, sleep spindles, and sensory
193 filtering[43], showed the most extensive translational reduction of *Gad2* (**Fig. 3g bottom row**),
194 correlated with the high abundance of PV neurons in this structure. Bulk analysis further revealed
195 translational downregulation of *Gad1* in the SSC (**Supplementary Table 5**), paralleling the
196 GABAergic dysfunction observed in human SCZ studies[37]. As further evidence of disturbed
197 GABAergic signaling in *Grin2a*+/- cortex, we observed translational upregulation of *Slc6a1*
198 (GAT1, mediates GABA reuptake from synaptic cleft) in both TEGLU and TEINH (**Fig. 3a,c**).
199 Beyond the GABAergic system, cortical inhibitory neurons also showed reduced translation of *Sst*
200 (somatostatin), *Cck* (cholecystokinin), and *Gnao1* (G-protein α subunit o) (**Fig. 3a,g**), particularly
201 in the superficial cortical layers, suggesting compromised signaling by Sst and Cck subtypes of
202 inhibitory interneurons and altered G-protein-mediated inhibitory modulation.

203 Besides reduced translation of key GABAergic-signaling related proteins in TEINH, our spatial
204 translatome profiling revealed additional evidence of disrupted inhibition in glutamatergic neurons
205 of the *Grin2a*+/- brain. In TEGLU, we observed robust translational downregulation (with minimal
206 to slight reduction of mRNA) of *Gabra1*, encoding the α1 subunit of GABAA receptors, suggesting
207 reduced responsiveness to inhibitory inputs to cortical pyramidal neurons (**Fig. 3a**). Translation
208 of *Gabra1* fell also in TEINH neurons (**Fig. 3c**). Of interest, previous studies of human SCZ brain
209 tissue also found reduced expression of GABRA1 in the prefrontal cortex[44]. Notably, we also
210 observed translational downregulation of carbonic anhydrase *Car2* in TEGLU, which may further
211 compromise GABAergic neurotransmission by reducing bicarbonate-dependent modulation of
212 GABAA receptor activity[45,46]. The widespread inhibitory dysfunction, combined with impaired
213 expression of plasticity- and glutamatergic synapse-related genes in TEGLU, suggests a
214 pathological microcircuit state in *Grin2a*+/- cortex characterized by weakened inhibitory control
215 over dysfunctional pyramidal neurons.

216 MSNs serve as the principal output cells of the basal ganglia, integrating excitatory inputs from
217 cortex and thalamus and dopamine input from substantia nigra and VTA to regulate movement,
218 reward-based learning, decision making, cognitive flexibility and motivation[47]. Direct pathway
219 MSN (MSN_1-[*Drd1_Rasd2*]) and indirect pathway MSN (MSN_2-[*Drd2_Penk*]) often work in
220 opposition to facilitate or suppress actions, respectively, and disruption of this balance has been
221 consistently implicated in SCZ[48,49]. In our dataset, both MSN subtypes showed translational
222 reduction of *Gad1* and *Gad2*, suggesting reduced GABA synthesis (**Fig. 3d, Supplementary**
223 **Table 4**). Beyond the shared reduction in GABA synthesis, MSN subtypes exhibited significant

224 translational downregulation of dopamine-receptor signaling pathways (**Fig. 4b**), including both
225 direct pathway (*Drd1*, *Ppp1r1b*) and indirect pathway (*Adora2a*) markers (**Fig. 3d,**
226 **Supplementary Table 4**). Notably, *Comt*, which catabolizes dopamine, showed translational
227 downregulation in line with the previous report showing downregulation of *Comt* at both mRNA
228 and protein levels[19]. Collectively, these data suggest reduced dopamine catabolism and perhaps
229 heightened dopamine signaling, accompanied by translational downregulation of dopamine
230 receptors in the striatum. Of particular interest, *Chrm1* and *Chrm4*, encoding the M1 and M4
231 muscarinic receptors and the target of Cobenfy, the recently FDA-approved SCZ drug, were
232 significantly downregulated in MSN_1 and MSN_2, respectively, suggesting disrupted cholinergic
233 signaling in the *Grin2a*+/- striatum (**Fig. 3d, Supplementary Table 4**). Moreover, translational
234 reduction of *Dlg2*, *Dlgap3*, *Nrxn2*, and *Synpo* suggests impact of *Grin2a*+/- on excitatory synapse
235 structure or function in MSNs.

236 As RIBOmap identified perturbations of multiple synaptic signaling and plasticity pathways, we
237 next performed quantitative mass-spectrometry (MS) proteomics on synaptic fractions (see
238 **Methods**) purified from the cortex of *Grin2a* LoF mutant mice to assess whether translational
239 alterations (RIBOmap) result in measurable protein-level changes at synapses. To better
240 compare with the synaptic proteome from bulk biochemical preparation, we generated
241 comparable STARmap and RIBOmap profiles combining reads from cell bodies and processes
242 (**Extended Data Fig. 5b-c, Supplementary Table 6**). We observed markedly higher
243 concordance between synaptic proteome profiling and RIBOmap than with STARmap in the
244 *Grin2a*+/- mutant (**Extended Data Fig. 5d,e**), with substantially more shared DEGs. Among the
245 RIBOmap DEGs showing significant changes in the synaptic proteome, 129 out of 197 and 181
246 out of 255 showed consistent direction in protein-level change in *Grin2a*+/- and *Grin2a*-/- mice,
247 respectively. Most shared DEGs were reduced in both datasets, particularly among postsynaptic
248 signaling, vesicle trafficking, and protein quality-control pathways. Notably, different isoforms of
249 the CAMKII complex (*Camk2a*, *Camk2b*, *Camk2g*) and multiple components of the ESCRT
250 complex (*Chmp3*, *Chmp4*, *Chmp2a*) were downregulated in the synaptic proteome of *Grin2a*+/-
251 or *Grin2a*-/- mutants, as well as in RIBOmap (*Grin2a*+/-), suggesting impaired postsynaptic
252 calcium-dependent signaling and membrane trafficking (**Extended Data Fig. 5d**). Similarly,
253 reduced translation and reduced protein levels of E3 ubiquitin ligases (*Pja1*, *Pja2*) and Hsp40 co-
254 chaperones (*Dnaja2*, *Dnaja4*) suggest compromised proteostasis and synaptic protein turnover.
255 Together, our cross-modal analysis (translatomics and proteomics) revealed that *Grin2a*
256 heterozygosity elicits major translational perturbations across diverse neuronal populations in a
257 cell-type- and brain-region-specific manner, ultimately driving changes in the level of key synaptic
258 proteins whose dysfunction could underlie the circuit aberrations of SCZ.

259 **Intrinsic *Grin2a* expression predicts vulnerability to LoF across neuronal subtypes**

260 Across neural subtypes, our spatial multi-omics approach revealed shared changes upon *Grin2a*
261 loss, particularly in RIBOmap (**Fig. 4a, Extended Data Fig. 6a-c**). A prominent pattern of

262 translational downregulation was observed for canonical activity-regulated genes[50] (ARGs) (*Egr1*,
263 *Egr3*, *Arc*, *Rheb*, *Nrn1*), ribosomal proteins (*Rpl13a*, *Rps24*, *Rpl32*), cytoplasmic signaling
264 proteins (*Rasgrp1*, *Rgs4*), and transcription/translation/metabolism regulators (*Ddx3x*, *Ell2*,
265 *Slc2a3*, *Scg2*) across multiple TEGLU and MSN subtypes (**Fig. 4a**). GSEA of RIBOmap data
266 confirmed broad translational downregulation of shared pathways not significantly altered at the
267 mRNA level (**Fig. 4b**). GO terms related to synapses, glutamatergic synaptic signaling,
268 translation, protein folding and transport, and oxidative phosphorylation were consistently
269 translationally downregulated across most neuronal subtypes. Spatial mapping of gene set score
270 differences further revealed that activity-related gene sets, ARGs and immediate early genes
271 (IEGs), were broadly reduced in RIBOmap across cortex and hippocampus, most prominently in
272 superficial cortical layers (**Extended Data Fig. 6d**). Meanwhile, oxidative phosphorylation and
273 ribosomal programs showed opposite regulation in RIBOmap in cortical regions versus striatum,
274 despite their mild upregulation in STARmap across most regions (**Extended Data Fig. 6d**),
275 suggesting region-specific translation control. These findings indicate that *Grin2a* loss disrupts
276 translation of a common set of genes and pathways critical for synaptic function and neuronal
277 activity, with magnitude varying across neuronal subtypes.

278 We next hypothesize that the magnitude of translational changes reflects the varying
279 dependencies of neuronal subtypes on *Grin2a* for maintaining their functional state. To test this,
280 we sought to correlate basal *Grin2a* expression in wild-type cells with RIBOmap log fold-changes
281 of individual DEGs across 15 neuronal subtypes. It was worth noting that TEGLU subtypes had
282 higher baseline *Grin2a* expression than other neuronal populations, with TEGLU_CA showing the
283 highest levels, while cortical TEGLU subtypes displayed a decreasing gradient of *Grin2a*
284 expression from superficial to deep layers (**Fig. 4c**). Next, we applied the Spearman's rank
285 correlation test to identify genes with RIBOmap log fold-change highly correlated with basal
286 *Grin2a* expression across neuronal subtypes (**Fig. 4d, Supplementary Table 7**). Our analysis
287 revealed a set of *Grin2a*-dependent genes with pathway-level associations, consisting of key
288 ARGs and synaptic plasticity regulators such as *Arc*, *Camk2a*, *Arhgef4*, *Chmp2b*, *Egr1*, *Egr3*, and
289 *Pja2* (**Fig. 4d, Extended Data Fig. 6e**). Specifically, we observed a quantitative relationship
290 where neuronal subtypes with higher basal *Grin2a* expression experienced greater translational
291 repression of these genes (**Fig. 4e**). From a spatial perspective, this subtype heterogeneity
292 indicated higher vulnerability of cortical layers and the hippocampus compared to subcortical
293 regions, aligning with gsMap (genetically informed spatial mapping of cells for complex traits)
294 prediction based on human genomics data[51] (**Extended Data Fig. 7**). In contrast, the correlation
295 between *Grin2a* basal expression and differential expression was weaker or absent in STARmap
296 data (**Fig. 4e**), particularly for *Camk2a*, *Egr1*, and *Egr3*, suggesting that the gene dosage effect
297 is primarily mediated at the translational level. *Arc*, however, showed significant correlation
298 between STARmap log fold-change and basal *Grin2a* expression, suggesting predominantly
299 transcriptional regulation. This set of *Grin2a*-dependent genes quantitatively links *Grin2a* dosage
300 to translational changes of downstream genes, partially explaining the heterogeneous effects of
301 *Grin2a* LoF across neuronal types.

302 **Transcriptional and translational changes in non-neuronal cell types of *Grin2a+/-* mice**

303 Glial and vascular cells also showed RIBOmap and STARmap changes in *Grin2a+/-* mutants (**Fig.**
304 **5a-d, Extended Data Fig. 8a**) presumably secondary to at least some neuronal alterations, as
305 *Grin2a* is expressed at low to minimal levels in non-neuronal cells (**Extended Data Fig.5a**).
306 Astrocytes showed translational reduction of GABA transporters *Slc6a11* and glutamate
307 transporter *Slc1a3*, suggesting altered clearance of inhibitory and excitatory neurotransmitters
308 (**Fig. 5a**). Key regulators of ionic and osmotic homeostasis, *Aqp4* and *Car2*, were downshifted at
309 the translational level, suggesting impaired water flux and pH buffering at astrocytic endfeet[52,53].
310 Moreover, genes involved in lipid/cholesterol synthesis (*Hmgcs1*, *Plpp3*, *Gpam*) and *Apoe*, were
311 downregulated in RIBOmap, suggesting translation reduction of astrocytic lipid/cholesterol
312 production and export. Notably, *Insig1*, a negative regulator of cholesterol synthesis, was
313 upregulated at the translational level, in line with mRNA upregulation of this gene observed in
314 previous snRNA-seq study[19]. GSEA results further revealed translational downregulation of
315 lipid/cholesterol metabolism, along with glutamate secretion and chaperone binding, in astrocytes
316 (**Fig. 5e**). Given that astrocytes are the major source of neuronal cholesterol, disrupted astrocytic
317 lipid supply could impair synaptic stability/function and membrane turnover in neurons[54,55].
318 Beyond this, we also observed altered translation of astrocytic genes involved in blood-brain
319 barrier function, including *Gja1*, *Hepacam*, *Vegfa*, and *Sema3g* (**Fig. 5a**).

320 In oligodendrocytes, RIBOmap also identified downregulation of genes involved in
321 lipid/cholesterol synthesis and transport (*Hmgcs1*, *Ugt8a*, *Apoe*, *Apod*, *Abcg1*), accompanied by
322 upregulation of *Insig1* and *Erlin2* (involved in cholesterol metabolism and ER stress response)
323 (**Fig 5b**). Lipids are important for myelin formation and integrity, as are tight junction protein
324 *Cldn11* and carbonic anhydrase *Car2*, which were also downregulated in RIBOmap, suggesting
325 compromised myelination in *Grin2a+/-* mutant brain[56]. In contrast, *Opalin*, an oligodendrocyte-
326 specific glycoprotein enriched at paranodal and inner myelin loops, was upregulated at both
327 mRNA and translational levels (**Fig. 5b**). Oligodendrocyte precursor cells (OPC) showed
328 translational downregulation of *Pdgfra*, a canonical marker and key regulator of OPC proliferation
329 (**Extended Data Fig. 8a**). Compared with astrocytes and oligodendrocytes, microglia showed
330 fewer translational changes, but purinergic receptor *P2ry12*, G protein-coupled receptor *Gpr34*,
331 fractalkine receptor *Cx3cr1*, and lysosomal protease *Ctss*, were downregulated in RIBOmap[57]
332 (**Extended Data Fig. 8a**).

333 Vascular cell populations, primarily pericytes and vascular endothelial cells, exhibited strong
334 concordance between transcriptional and translational changes for upregulated DEGs (**Fig. 5c,d**),
335 including glucose transporter *Slc2a1*, angiogenesis regulator *Apold1*, and extracellular-matrix
336 regulators *Adamts1* and *Timp3*. Interestingly, IEGs (*Btg2*, *Jun*, *Junb*, *Klf10*, *Nr4a1*) and stress-
337 responsive regulators[58–60] (*Tnfrsf12a*, *Akap12*, *Tsc22d3*) were elevated at both mRNA and
338 translational levels. Among the translationally downregulated genes, carbonic anhydrase *Car4*
339 and tight junction protein *Cldn5* stood out, suggesting perturbation of perivascular pH
340 homeostasis and blood-brain barrier integrity. Moreover, GSEA suggested translational

341 downregulation of the tight-junction pathway in vascular cells (**Fig. 5e**). At the transcriptional level,
342 pericytes displayed the strongest signals associated with apoptosis, fibroblast migration, and
343 nutrient-stress pathways (**Fig. 5e**). Together, these findings suggest vascular stress and altered
344 blood brain barrier function in *Grin2a+/-* brain.

345 Additionally, we observed significant differences in DEG profiles among subtypes of astrocytes
346 and oligodendrocytes (**Extended Data Fig. 8b,c**), each characterized by unique marker genes
347 and distinct spatial distributions (**Fig. 5f**). Specifically, AC_2-[*Cspg5_Mfge8*], located within
348 cortico-striatal and hippocampal regions (where neurons showed translational changes in
349 numerous genes including ARGs) showed the highest number of DEGs among astrocyte
350 subtypes (**Extended Data Fig. 8b**). In contrast, white-matter localized AC_3-[*Gfap_Aqp4*], with
351 little local contact with neurons, showed significantly fewer DEGs at both mRNA and translational
352 levels. Similarly, the white-matter-localized oligodendrocyte subtype (OLG_3) showed the least
353 transcriptional and translational changes among all three subtypes (**Extended Data Fig. 8c**).
354 These data further support the notion that, in *Grin2a* +/- animals, glial alterations are secondary
355 to initiating changes in local neurons, where *Grin2a* is primarily expressed. Analyses by snRNA-
356 seq of human postmortem prefrontal cortex have revealed concerted regulation of a synaptic
357 neuron and astrocyte program (SNAP), which is under-expressed in SCZ patients[61]; we
358 calculated SNAP scores (using the mouse orthologs of these human genes) for astrocytes
359 (SNAP-a) and neurons (SNAP-n) to test whether such a concerted downregulation also occurs in
360 *Grin2a+/-* mouse. Indeed, all cortical TEGLU subtypes showed significant translational reduction
361 of the SNAP-n program, consistent with the idea that decline in SNAP disrupts the synaptic
362 proteome; we also observed significant translational reduction of the SNAP-a program in AC_1
363 and AC_2 (grey matter astrocytes), but not in AC_3 (white matter astrocytes) (**Fig. 5g**).
364 Furthermore, the RIBOmap-measured changes of SNAP-a and SNAP-n showed striking
365 similarities in their spatial distributions, consistent with the idea that they are coordinated (**Fig.
366 5h**). Both SNAP-a and SNAP-n exhibited the greatest reduction in the insular cortex (CTX_AI2/3),
367 a brain region responsible for processing sensory stimuli and highly affected in SCZ[62], and were
368 more downregulated in the prefrontal cortex and the striatum compared to the somatosensory
369 cortex and thalamus. In comparison, STARmap captured little evidence of astrocyte-neuron
370 coordination: SNAP-a was decreased in all astrocyte subtypes while SNAP-n was significantly
371 changed only in TEGLU_L4/5 (upregulated) (**Extended Data Fig. 8d,e**). Thus, both cell-subtype
372 and spatial analyses suggest coordinated regulation between neuronal synaptic function and local
373 astrocyte support manifests at translational level and is undermined by *Grin2a*+/-.

374 **Co-variation of translatomic changes among neurons and non-neuronal cell types across
375 brain regions in *Grin2a*+/- mice**

376 Leveraging the spatial resolution of RIBOmap data, we next examined whether different brain cell
377 types within the same tissue region have coordinated translatome changes. To this end, we first
378 computed region-specific RIBOmap log fold-changes of selected DEGs from four abundant cell
379 populations, including neurons (169 DEGs shared between at least 3 neuronal subtypes),

380 astrocytes (64 DEGs), oligodendrocytes (56 DEGs), and pericytes (39 DEGs) (**Supplementary**
381 **Table 8**). Five molecular tissue regions (VS, FT, MNG, CTX_HIP, CTX_PIR) were excluded from
382 the analysis due to low neuron abundance, leaving 18 regions for downstream correlation
383 analysis. We computed Pearson's correlation coefficients for all possible cross-cell-type DEG
384 pairs across these regions as a metric of gene-gene co-variation. Our analysis revealed significant
385 co-variations between neuronal and non-neuronal DEGs (**Fig. 6a**): 219 neuron-astrocyte pairs,
386 56 neuron-oligodendrocyte pairs, and 39 neuron-pericyte pairs exhibited strong co-variation
387 (|Pearson's r|>0.8). In addition, we identified 22 highly correlated DEG pairs among different non-
388 neuronal cell types: 10 between astrocytes and oligodendrocytes, 7 between astrocytes and
389 pericytes, and 5 between oligodendrocytes and pericytes (**Fig. 6a**).

390 Notably, astrocytes exhibited the most extensive gene-gene translational co-variations with
391 neurons (**Fig. 6a**), consistent with their role in supporting and responding to synapses[63,64]. Given
392 that the neurovascular unit (NVU) relies on interplay between neurons, astrocytes, and vascular
393 cells[65], we next examined whether cross-cell-type co-variations exist among NVU-related genes
394 and indeed found a dense interaction network linking neuronal, astrocytic, and pericytic NVU-
395 associated DEGs (**Extended Data Fig. 9a,b**). In particular, the astrocytic glutamate transporter
396 *Slc1a3* (encoding EAAT1) showed high correlation with vesicular glutamate transporter *Slc17a7*
397 and multiple genes in NMDAR-dependent signaling pathways (*Camk1*, *Ppp3ca*, *Arc*) (**Extended**
398 **Data Fig. 9a**), suggesting that regional changes in astrocytic glutamate clearance are coordinated
399 with local glutamatergic signaling-associated changes in neurons. Other representative co-varied
400 DEG pairs included *Camk1* (neuron) with *Slc1a3* (astrocyte), *Egr3* (neuron) with *Htra1* (astrocyte),
401 *Atp1a1* (neuron) with *Spock2* (pericyte), and *Vegfa* (astrocyte) with *Timp3* (pericyte) (**Extended**
402 **Data Fig. 9b**). These patterns suggest that translational shifts in neurons, astrocytes, and
403 pericytes are interlocked, coordinating neuron state with glial and vascular support.

404 To pinpoint glial DEGs with direct relevance to local neuronal activity-associated gene programs,
405 we first derived a "neuronal activity index" for each region by calculating the mean gene group
406 score of IEGs by RIBOmap in neurons. We then correlated the regional change in neuronal IEG
407 score with the log fold-change of every glial DEG, using Spearman's rank correlation to capture
408 monotonic relationships (**Fig. 6b**). This analysis revealed a set of glial RIBOmap DEGs (13
409 astrocyte DEGs, 5 oligodendrocyte DEGs) that appear coupled to neuronal activity, such as
410 *Insig1*, *Slco1c1*, *Vegfa*, *Slc1a3*, and *Htra1* in astrocytes, and *Cldn11*, *Car2* in oligodendrocytes.
411 Interestingly, *Slco1c1* and *Vegfa* were previously identified as astrocytic activity-response genes
412 (AAR genes) in neuron-astrocyte co-culture systems, which corroborates our discovery of their
413 gene-activity co-variation in brain tissues[66]. In cortical areas, where neuronal activity-associated
414 programs show prominent translational changes, these glial activity-coupled genes tend to show
415 greater differential expression (**Fig. 6c,d**). For example, astrocytes suppress *Slco1c1*, *Slc1a3*,
416 and upregulate *Insig1*, while oligodendrocytes downregulate *Car2* (**Fig. 6d**). This concerted
417 modulation implies a stronger cortical disruption of lipid metabolism, neurotransmitter clearance,
418 and pH-buffering. In contrast, in thalamic regions where neuronal activity-associated programs
419 showed subtle changes, modest differential expressions were observed for the same genes.

420 Notably, the neuron-activity-coupled astrocytic translation shift of *Insig1* paralleled human
421 schizophrenia snRNA-seq findings showing downregulation of astrocytic cholesterol biosynthetic
422 genes in correlation with reduced neuronal activity markers[61]. Together, these findings indicate
423 that glial support programs are not uniformly changed across the brain in *Grin2a*+/- mutants but
424 instead scale translationally with local neuron state changes as measured by RIBOmap.

425

426 **Discussion**

427 By integrating spatially resolved transcriptomic and translatomic technologies, we revealed
428 pronounced translational dysregulation across the *Grin2a*+/- mutant brain with striking cell-type
429 and regional heterogeneity. In fact, numerous RIBOmap DEGs showed marked changes in
430 translation but little change in mRNA level (*Ppp3ca*, *Gabra1*, *Gad2*, *Rheb*, *Camk2a*, *Nrn1* being
431 interesting examples). Our findings underscore the critical role of translational control in brain
432 function and SCZ pathophysiology and highlight an important regulatory mechanism that is quite
433 overlooked in transcriptome-only studies.

434 Our study uncovered translational dysregulation of excitatory and inhibitory neurotransmission in
435 major neuron cell types, including glutamatergic, GABAergic, and striatal dopaminergic signaling.
436 Moreover, we identified pervasive translational suppression of calcium-dependent synaptic
437 plasticity regulators across multiple neuronal subtypes, including *Arc*, *Egr1*, *Rheb*, *Camk2a*, and
438 *Ppp3ca*, which may contribute to SCZ-associated deficits in learning and memory processes. By
439 comparing RIBOmap with synaptic proteomics, we identified a set of RIBOmap DEGs and
440 synaptic DEPs that change in the same direction and are known to act in synaptic function and
441 plasticity, including CAMKII isoforms, ESCRT-associated endosomal sorting factors, E3 ubiquitin
442 ligases, and Hsp40 co-chaperones. Our results suggest that the compromised protein levels of
443 these genes at synapses is driven by translational suppression of their mRNAs, rather than by
444 reduced mRNA levels.

445 RIBOmap was also able to uncover prominent alterations in inhibitory interneurons (TEINH) that
446 were absent in STARmap and that were largely missed by previous snRNAseq analysis of
447 *Grin2a*+/- brain[19]. Notably, reduced translation of GABA synthesizing enzyme *Gad2* in different
448 TEINH subtypes, most prominently in PV interneurons (**Extended Data Fig. 6b**), as well as
449 downregulation of neuropeptides cholecystokinin (*Cck*) and somatostatin (*Sst*) which are primarily
450 expressed by inhibitory interneurons (**Fig. 3c**) suggests disrupted inhibitory interneuron function.
451 Our findings in TEINH are reminiscent of human postmortem SCZ studies, which also uncovered
452 reduced expression of GAD in PV interneurons of prefrontal cortex[36,38,39], and are in keeping with
453 a long-standing theory for the cognitive impairment of SCZ[37]. Thus, together with our prior
454 transcriptomic study[19], the current data show evidence in support of the three major hypotheses
455 for the pathophysiology of SCZ in *Grin2a*+/- mice: hypoglutamatergic function[15,16];
456 hyperdopaminergic signaling in the striatum[67]; and inhibitory interneuron dysfunction in the
457 neocortex[37,38].

458 By correlating baseline *Grin2a* expression with translational changes across 15 neuronal
459 subtypes, we provided key molecular insights into cell autonomous impacts of *Grin2a* LoF on
460 downstream genes. We identified a set of genes, including *Camk2a*, *Arc*, *Egr1*, *Egr3*, *Chmp2b*,
461 and *Pja2*, whose translational suppression was highly correlated with basal (WT) expression of
462 *Grin2a* across neuronal subtypes, with this dosage effect operating primarily translationally rather
463 than transcriptionally. Cortical and hippocampal TEGLU with the highest basal *Grin2a* expression
464 exhibited the greatest translational dysregulation of these genes, which aligns with these cell-
465 types' particularly strong association with human SCZ traits[51] (**Fig. 4c,d**, **Extended Data Fig. 7**),
466 demonstrating high human SCZ-relevance of our finding.

467 Beyond neurons, our study revealed distinct and region-specific translational alterations in non-
468 neuronal cell types. In RIBOmap, astrocytes showed translational downregulation of
469 neurotransmitter transporters and lipid/cholesterol metabolism genes, indicating compromised
470 synaptic support, particularly in cortical regions. Oligodendrocytes exhibited dysregulated lipid
471 metabolism and myelin integrity maintenance. It is noteworthy that no significant STARmap
472 changes were observed for most RIBOmap DEGs in the aforementioned pathways, suggesting
473 RIBOmap (translatomic profiling) is more capable of detecting differential expression indicative of
474 functional changes also in glial cell types. Meanwhile, vascular cells upregulated stress-response
475 and extracellular matrix remodeling programs. Given that these non-neuronal cell types express
476 *Grin2a* at low to minimal levels, we reason that the translatomic changes in these cells are
477 secondary to changes in neurons.
478
479 The spatial resolution of STARmap and RIBOmap allows us to uncover regional heterogeneity in
480 cell-cell interactions that would have been missed by bulk approaches. Across 18 molecular tissue
481 regions, we revealed striking cross-cell-type DEG co-variations between neurons, astrocytes,
482 oligodendrocytes, and pericytes, particularly among NVU-associated genes. Additionally, we
483 discovered astrocyte and oligodendrocyte DEGs that co-varied with RIBOmap IEG score in
484 neurons in the local region. These findings highlight a coordinated local response to NMDAR
485 hypofunction, where glial support programs scale with local neuronal circuit disturbance.
486
487 Furthermore, our study bridges the findings in *Grin2a*+/- mouse model with previous
488 characterization of human SCZ patients. At subcellular level, we identified key RIBOmap DEGs,
489 such as *Grin1* and *Homer1*, that also show significant reduction in synaptic proteome of human
490 SCZ samples[68,69]. At cell-cell interaction level, we observed a concerted disruption of the neuron-
491 astrocyte program SNAP, a gene set showing concerted downregulation in postmortem prefrontal
492 cortex of SCZ patients. At the brain-region level, we identified prominently affected regions in
493 *Grin2a*+/- model, such as superficial cortical layers, prefrontal cortex, insular cortex, and thalamic
494 reticular nucleus, which aligns with computational predictions based on human genetics data
495 (**Extended Data Fig. 7b**). These consistencies largely reinforce the disease relevance of our
496 findings in the *Grin2a*+/- model.

497 In summary, our integrated spatial omics analysis shows that *Grin2a* haploinsufficiency drives
498 brain-wide translational shifts in all cell types examined. Translational reduction in calcium-
499 dependent synaptic plasticity and neurotransmission appears to be a widespread consequence
500 of NMDAR hypofunction in both excitatory and inhibitory neurons, along with further cell-type and
501 region-specific adaptations across neurons, glia, and vascular cells. Given the prominent
502 translational dysregulation of *Grin2a*+/- model, our study inspires future applications of RIBOmap
503 to explore the spatial molecular changes in other SCZ disease models and human patient
504 samples.

505 **Methods**

506 **Mouse brain tissue collection**

507 All animal procedures followed animal care guidelines approved by the Institutional Animal Care
508 and Use Committee (IACUC) at the Broad Institute of MIT and Harvard. Male *Grin2a*+/- and wild-
509 type littermate mice were anesthetized with isoflurane, perfused with PBS, and decapitated at 12
510 weeks of age. Brains were rapidly extracted, snap freezed in O.C.T. with liquid nitrogen, and
511 stored at -80 °C.

512 **STARmap and RIBOmap**

513 We employed paired primer and padlock probes in STARmap to detect mRNA irrespective of its
514 translational state, whereas a combination of splint, primer, and padlock probes was used in
515 RIBOmap to specifically identify ribosome-bound mRNA[5].

516 In detail, mouse brain samples were sectioned at 20 μm thickness on Leica Cm1950 cryostat at
517 -20 °C. For each animal, 6 coronal sections, including 2 adjacent sections at each of the 3 coronal
518 positions, were prepared and transferred to 24-well glass-bottom plates (Cellvis). Plates were pre-
519 treated by oxygen plasma cleaning, followed by bind-silane coating (10% acetic acid, 1%
520 methacryloxypropyltrimethoxysilane, 89% ethanol; 1 h, room temperature). Plates were rinsed
521 three times with 95% ethanol, air-dried, and coated with 50 μg/mL poly-D-lysine (1 h, room
522 temperature). Tissue sections were fixed in 4% paraformaldehyde (PFA) in PBS (15 min, room
523 temperature) and permeabilized in pre-chilled methanol (–20 °C, 1 h). Sections were then
524 quenched in PBSTR buffer (0.1% Tween-20, 0.1 U/μL RNase inhibitor in PBS) supplemented with
525 1% yeast tRNA and 100 mM glycine (5 min, room temperature), followed by rinsing in PBSTR.

526 For STARmap and RIBOmap hybridization, probe mixtures were prepared by combining equal
527 volumes of diluted probe solution (padlock and primer probes, 2 nM per oligo) with hybridization
528 buffer (4x SSC, 20% formamide, 2% Tween-20, 40 mM ribonucleoside vanadyl complex, 0.2
529 mg/mL yeast tRNA, 0.4 U/μL SUPERase inhibitor), yielding a final probe concentration of 1 nM
530 per oligo. For RIBOmap, an additional splint probe (100 nM final concentration) was included.
531 Sections were incubated in a hybridization mixture at 40 °C in a humidified chamber with gentle

532 shaking and parafilm sealing for 36 h. Excess probes were removed by two PBSTR washes
533 followed by a high-salt wash (4x SSC in PBSTR) at 37 °C for 20 min each.

534 Padlock ligation was performed in T4 DNA ligase buffer containing 0.5 mg/mL BSA, 0.2 U/μL
535 RNase inhibitor, and 0.25 U/μL T4 DNA ligase (3 h, room temperature), followed by 3 PBSTR
536 washes. Following ligation, sections were incubated in rolling circle amplification (RCA) solution
537 consisting of 0.5 U/μL Phi29 DNA polymerase, 250 μM dNTPs, 20 μM 5-(3-aminoallyl)-dUTP, 0.2
538 mg/mL BSA, and 0.2 U/μL RNase inhibitor in Phi29 buffer. Samples were preincubated at 4 °C
539 for 30 min, then transferred to 30 °C for 2 h with gentle shaking, and subsequently washed twice
540 in PBST (0.1% Tween-20 in PBS).

541 For hydrogel embedding, sections were treated with modification solution (25 mM methylacrylic
542 acid NHS ester in 100 mM sodium bicarbonate) for 1 h at room temperature, rinsed twice in PBST,
543 and incubated in monomer buffer (4% acrylamide, 0.2% bis-acrylamide, 2x SSC, 0.2% TEMED)
544 for 10 min at 4 °C. The buffer was removed, and 40 μL of polymerization mixture (0.2% ammonium
545 persulfate in monomer buffer) was applied to each section. Gel Slick-coated coverslips were
546 placed immediately over the samples, and polymerization proceeded for 1.5 h at room
547 temperature under a nitrogen atmosphere. Coverslips were carefully removed, and hydrogels
548 were washed twice in PBST. Sections were digested in proteinase K solution (0.2 mg/mL
549 proteinase K, 1% SDS, 2x SSC) at 37 °C for 1 h, followed by PBST washes. Dephosphorylation
550 was performed in Antarctic phosphatase buffer containing 0.25 U/μL Antarctic phosphatase and
551 0.2 mg/mL BSA at 37 °C for 1 h, followed by PBST washes.

552 Each SEDAL cycle began with two 10 min treatments at room temperature in stripping buffer
553 (60% formamide, 0.1% Triton X-100), followed by three 5 min PBST washes. Samples were then
554 incubated for 3 h at room temperature in sequencing buffer (1x T4 DNA ligase buffer, 0.2 mg/mL
555 BSA, 10 μM reading probe, 5 μM fluorescent decoding probe, 0.2 U/μL T4 DNA ligase). After
556 incubation, samples were washed three times with imaging buffer (2x SSC, 10% formamide) and
557 maintained in the same buffer during imaging. DAPI staining was performed prior to the first
558 sequencing cycle for 3 h.

559 Imaging was carried out on a Leica TCS SP8 confocal microscope equipped with a 40x oil-
560 immersion objective. For each cycle, signals were acquired in Alexa Fluor 488, 546, 594, and 647
561 channels. DAPI signals were collected in the first cycle using a 405 nm laser. A total of 8
562 sequencing-imaging cycles were conducted, enabling the detection of 3,447 target genes.

563 **5' phosphorylated padlock library preparation**

564 The padlock probe library was synthesized by IDT oPool service without 5' phosphorylation. A
565 common annealing site was added to the 5' end of all padlock probe sequences (STARmap
566 padlocks: TAATACGACTCACTATACTGCTAGCGACGGCCA; RIBOmap padlocks:
567 TAATACGACTCACTATACTGCTAGATAACACGGCCT). The probe pool was then cleaved by a
568 13PD-1 DNAzyme cutter oligo (STARmap:
569 AAAAAAAAAAAATGGCCGTCGCTTATACCGGGCAACTATTGCCTCGTCATCGCTATTTTCTG

570 CGATAGTGAGTCGTATTAAAAAAAAAAAAA, RIBOmap:
571 AAAAAAAAAAAAAAGGCCGTGTTATCTTATACCGGGCAACTATTGCCTCGTCATCGCTATTTT
572 CTGCGATAGTGAGTCGTATTAAAAAAAAAAAAA) at a final concentration of 100 nM in the
573 annealing buffer containing 50 mM HEPES (pH 7.0 at 22 °C), 100 mM NaCl, and 10 mM $MgCl_2$.
574 The mixture was incubated on a thermocycler at 90 °C for 3 min and cooled to 25 °C at a rate of
575 -0.1 °C/s, and then an equal volume of the cutting buffer (50 mM pH 7.0 HEPES, 100

576 mM NaCl, 10 mM $MgCl_2$, 10 mM $MnCl_2$, and 4 mM $ZnCl_2$) was added. The reaction was then
577 incubated at 37 °C to allow DNAzyme-assisted autocleavage to yield a 5' phosphate moiety on
578 the padlock probes. The reaction was then quenched by 0.5 M EDTA. The oligos were ethanol
579 precipitated, and the 5' phosphorylated padlock pools were isolated on an Agilent 1260 Infinity II
580 HPLC with acetonitrile/hexylamine/acetic acid (pH 7.0) mobile phase and PLRP-S stationary
581 phase. The purified 5' phosphorylated padlocks were pooled, desalted, ethanol precipitated, and
582 resuspended in 0.1 TE buffer, and the concentration of probes was quantified by Qubit ssDNA
583 assay.

584 **Imaging Data Processing**

585 Image deconvolution was achieved with Huygens Essential version 24.04 (Scientific Volume
586 Imaging, The Netherlands, http://svi.nl), using the CMLE algorithm, with SNR:10 and 10 iterations.
587 Image registration, spot calling, and barcode filtering were performed using established software
588 Starfinder (https://github.com/wanglab-broad/starfinder) with customized configuration.

589 **Quality control and preprocessing**

590 After quantifying signals at the single-cell level, we excluded low-quality cells from each replicate
591 based on the number of transcripts and genes per cell. We used the median absolute deviation
592 (MAD) to establish filtering thresholds for reads per cell:

593 $$lower\ boundary = median(reads\ per\ cell) - 3 \times MAD$$

594 $$upper\ boundary = median(reads\ per\ cell) + 3 \times MAD$$

595 Additionally, we applied standard filtering criteria: 1) A minimum of 10 expressed genes is required
596 for a cell to pass filtering. 2) A minimum of 10 expressing cells is required for a gene to pass
597 filtering. Following these filters, we retained a total of 538,188 cells with 3,447 genes. The
598 expression profiles were normalized using the pp.normalize_total function (Scanpy v1.9.2),
599 followed by logarithmic transformation with pp.log1p. We scaled the data matrix to unit variance
600 using pp.scale and mitigated variations in total reads per cell with pp.regress_out. Finally, to
601 ensure a high-quality cell-typing, we selected 1,017 canonical cell type markers from previous
602 reports to perform a Harmony integration on the processed data matrix to align transcriptome and
603 translatome modalities before conducting downstream analyses such as dimensionality reduction
604 and unsupervised clustering.

605 **Cell type classification**

606 We applied a hierarchical clustering strategy to create a three-level cell-type annotation for the
607 integrated dataset. First, we constructed a k-nearest neighbor (k-NN) graph from the integrated
608 PCA matrix, connecting cells based on their expression similarity in high-dimensional space. We
609 then used the Leiden community detection algorithm on this k-NN graph to identify cell clusters,
610 resulting in twenty-eight clusters at a clustering resolution of 2. Each cluster was classified as
611 either neuron or glial cell based on canonical markers (e.g., *Slc17a7*, *Gad1*, *Gad2*, *Plp1*, *Slc1a3*).
612 Subsequently, we generated second-level annotations reflecting major cell types such as
613 telencephalon projecting neurons, oligodendrocytes, astrocytes, and vascular cells.

614 To identify subpopulations of major cell types, we applied the same analyses to various
615 populations under second-level annotation (e.g., telencephalon projecting neurons and
616 interneurons). We used the elbow method to determine significant principal components after
617 performing PCA. By plotting the variance ratio of each principal component with the
618 pl.pca_variance_ratio function, we selected the top 10 to 30 components with the highest values
619 for constructing a kNN graph for clustering. Specifically, eleven clusters were first identified from
620 the telencephalon projecting neurons (TEGLU). The subpopulations located in the hippocampal
621 and cortical regions were then subject to unsupervised clustering again to differentiate neuronal
622 subtypes with distinct spatial representation in the brain regions (i.e., anatomical regions such as
623 L2/3, L4/5, CA, DG, etc.), resulting in seven subpopulations with unique representative gene
624 markers. For inhibitory interneurons, we resolved four clusters distinguished by different neuronal
625 peptide gene markers (e.g., *Pvalb*, *Sst,* and *Vip*). In non-neuronal cells, we identified three
626 subpopulations each from oligodendrocytes and astrocytes, along with five from vascular cells.
627 Additionally, cells without conventional maker expression were labeled as mixed cells and
628 excluded from downstream cell-type-specific analyses.

629 **Molecular tissue region identification**

630 Tissue region annotation was performed using the SPIN algorithm, which combines single-cell
631 gene expression similarity and spatial proximity to identify tissue regions. Gene expression
632 features for each cell were averaged from a subsampled set of its spatial neighbors. These
633 smoothed features were then clustered using the Leiden algorithm at a resolution of 0.7,
634 producing distinct molecular regions, where most identified regions had representative gene
635 markers. Anatomical labels were then assigned by overlaying these regions with the Allen
636 Mouse Brain Atlas and comparing with the Spatial Mouse Brain Atlas in Shi et al. Finally, the
637 annotated cells were further refined using kNN majority voting (n_neighbors=50) to create
638 clearer tissue boundaries.

639 **Consensus non-negative matrix factorization (cNMF)**

640 cNMF (v.1.7) was applied to the integrated dataset following the PBMC tutorial on GitHub
641 (https://github.com/dylkot/cNMF/blob/master/Tutorials/analyze_pbmc_example_data.ipynb).
642 Factorization was performed on filtered raw counts data, iterating over k values from 30 to 40.
643 Based on the PCA of the gene expression matrix and the cNMF stability report, we selected k =

35 with a density threshold of 0.2 for further analysis. Additionally, the latent factor usage matrix (cell by factor) was normalized so that each cell's total usage across all factors summed to one before analysis. With each module, top 50 genes were subjected to downstream analysis.

**Differential gene expression analysis**

Differential expression (DE) analysis was conducted using the sc.tl.rank_genes_groups function in Scanpy, employing the Wilcoxon rank-sum test. Comparisons were made between genotypes within each cell type, retaining only genes with an absolute log fold-change ($\log_2$FC) of 0.2 or greater and a Benjamini-Hochberg-adjusted p-value lower than 0.05. To ensure consistency across biological replicates, we applied a filter that included only genes exhibiting changes in the same direction. To ensure cell type specificity, we further applied a filter based on cNMF gene modules to exclude glial DEGs that are potentially dominated by mis-segmented reads from neuronal processes.

**Gene set enrichment analysis**

The Enrichr API in the GSEApy library was utilized to evaluate the functional enrichment of cNMF modules using the top 50 highest-ranking genes from each module, with the complete gene panel serving as the background. We selected terms with an adjusted p-value below 0.05 and a size greater than 2. Additionally, we conducted Gene Set Enrichment Analysis (GSEA) for neuronal and glial subtypes using gene sets from Farsi *et al*., which included the C5 v7.2 collection (comprising 14,765 Gene Ontology terms) from the Molecular Signature Database (http://www.gsea-msigdb.org/gsea/msigdb), SynGO collection, and other literature-derived gene sets. Terms were chosen based on an FDR q-value below 0.05 and meeting expression thresholds.

**Cross-cell-type correlation analysis**

For neuronal, astrocyte, oligodendrocyte, and pericyte DEGs, we computed regional log fold-changes for each gene across 18 molecular tissue regions identified by SPIN. 5 molecular tissue regions (VS, FT, MNG, CTX_HIP, CTX_PIR) were excluded from the analysis due to low neuron abundance. Pearson correlation coefficients were then calculated for every possible cross-cell-type DEG pair, yielding full cross–cell-type correlation matrices for downstream analyses. In parallel, regional neuronal immediate early gene (IEG) score changes were calculated and correlated with glial DEGs to identify glial genes associated with neuronal activity.

**Mapping human GWAS traits with gsMap**

gsMap (v1.73.6) was applied to each WT sample to generate single-cell association scores with GWAS traits associated with human schizophrenia, following the GitHub tutorial (https://yanglab.westlake.edu.cn/gps_data/website_docs/html/tutorials.html). Each sample was processed in quick mode using default settings, with an added uniform slice mean to account for multiple biological replicates.

680 **Purification of synapse fractions**

681 Whole cortices from 4-week and 12-week old male Grin2a mutant mice and wild-type littermates
682 (n=5 wild-type, 5 heterozygous knockouts, 5 homozygous knockouts of each age) were used in
683 this study. Mice were euthanized by $CO_2$ inhalation, after which the cortex was rapidly dissected,
684 flash-frozen in liquid nitrogen, and stored at −80 °C until processing.

685 Synapse fractions were purified as previously described[68,70]. Briefly, frozen cortex tissue was
686 thawed on ice and dounce-homogenized in ice-cold homogenization buffer (5 mM HEPES pH
687 7.4, 1 mM $MgCl_2$, 0.5 mM $CaCl_2$, supplemented with protease and phosphatase inhibitors). The
688 homogenate was centrifuged at 1,400 g for 10 min at 4 °C, and the resulting supernatant was
689 centrifuged again at 13,800 g for 10 min at 4 °C. The pellet was resuspended in 0.32 M sucrose,
690 6 mM Tris-HCl (pH 7.5), layered onto a discontinuous sucrose gradient (0.85 M, 1.0 M, and 1.2
691 M sucrose in 6 mM Tris-HCl pH 7.5), and ultracentrifuged at 82,500 g for 2 h at 4 °C.

692 The synaptosome fraction, located at the interface between the 1.0 M and 1.2 M sucrose layers,
693 was collected and mixed with an equal volume of ice-cold 1% Triton X-100 (in 6 mM Tris-HCl pH
694 7.5). After incubation on ice for 15 min, the sample was ultracentrifuged at 32,800 g for 20 min at
695 4 °C. The resulting pellet was solubilized and resuspended in 1% SDS in H2O. This pellet is highly
696 enriched for postsynaptic density proteins, as well as for proteins of the cytomatrix of the active
697 zone (CAZ). Although this fraction has historically been referred to as the “postsynaptic density”
698 fraction, we refer to it as the “synapse fraction” to reflect the abundant presence of CAZ
699 proteins68. After solubilization, a small aliquot was removed for protein quantification by BCA
700 assay (Thermo Fisher Scientific), and the remaining material was stored at −80 °C until
701 quantitative mass spectrometry.

702 **Processing of synapse fractions for mass spectrometry (MS/MS)**

703 The protein in synapse fraction samples from both 4-week and 12-week animals (in 1% SDS) was
704 reduced using 5 mM dithiothreitol and alkylated using 10 mM iodoacetamide at room temperature.
705 The denatured, reduced, alkylated protein samples were then processed using S-Trap sample
706 processing technology (Protifi) following manufacturer’s instructions. The proteins were bound to
707 the S-Trap column via centrifugation and contaminants/detergents were washed away.
708 Sequential digestion steps were then performed on column using 1:20 enzyme to substrate ratio
709 of Lys-C for 2 hours followed by Trypsin overnight at room temperature.

710 Two Tandem Mass Tag (TMT) 16-plex experiments were constructed, each containing samples
711 from the same age group. Additionally, a pooled reference sample was created using equal
712 amounts of all 30 (15 4-week and 15 12-week) samples to include in each plex for cross-plex
713 comparison. Following digestion, 50 µg of each sample was labeled with TMT16 reagent. Each
714 plex included five wild-type, five *Grin2a*+/-, and five *Grin2a*-/- samples, which were randomly
715 assigned to TMT reporter channels. The last channel 134N contained the pooled reference
716 sample in both plexes. After verifying successful labeling of more than 95% label incorporation,
717 reactions were quenched using 5% hydroxylamine and samples were mixed together. The TMT16

718 labeled peptides were desalted on a 50 mg tC18 SepPak cartridge and fractionated by high pH
719 reversed-phase chromatography on a 4.6 mm x 250 mm Zorbax 300 extend-c18 column (Agilent).
720 One-minute fractions were collected during the entire elution and fractions were concatenated
721 into 12 fractions for LC-MS/MS analysis.

722 **Liquid chromatography- Mass Spectrometry analysis (LC-MS/MS)**

723 One microgram of each proteome fraction was analyzed on a QE-HFX mass spectrometer
724 (Thermo Fisher Scientific) coupled to an easynLC 1200 LC system (Thermo Fisher Scientific).
725 Samples were separated using 0.1% Formic acid / 3% Acetonitrile as buffer A and 0.1% Formic
726 acid / 90% Acetonitrile as buffer B on a 27cm 75um ID picofrit column packed in-house with
727 Reprosil C18-AQ 1.9 mm beads (Dr Maisch GmbH) with a 110 min gradient consisting of 2-6% B
728 in 1 min, 6-20% B in 62 min, 20-30% B for 22 min, 30-60% B in 9 min, 60-90% B for 1 min followed
729 by a hold at 90% B for 5 min. The MS method consisted of a full MS scan at 60,000 resolution
730 and an AGC target of 3e6 from 350-1800 m/z followed by MS2 scans collected at 45,000
731 resolution with an AGC target of 1e5 with a maximum injection time of 105 ms and a dynamic
732 exclusion of 15 seconds. The isolation window used for MS2 acquisition was 0.7 m/z and 20 most
733 abundant precursor ions were fragmented with a normalized collision energy (NCE) of 29
734 optimized for TMT16 data collection.

735 **Database search and MS/MS quantification**

736 The data was analyzed using Spectrum Mill MS Proteomics Software (Broad Institute) with a
737 mouse database from Uniprot.org downloaded on 04/07/2021 and containing 55,734 entries.
738 Proteins identified by one or more peptides were selected for further analysis. Search parameters
739 included: ESI Q Exactive HCD v4 35 scoring parent and fragment mass tolerance of 20 ppm, 40%
740 minimum matched peak intensity, trypsin allow P enzyme specificity with up to four missed
741 cleavages, and calculate reversed database scores enabled. Fixed modifications were
742 carbamidomethylation at cysteine. TMT labeling was required at lysine, but peptide N termini
743 could be labeled or unlabeled. Allowed variable modifications were protein N-terminal acetylation,
744 deamidation and methionine oxidation. Protein quantification was achieved by taking the ratio of
745 TMT reporter ions for each sample over the TMT reporter ion for the pooled reference channel.
746 TMT16 reporter ion intensities were corrected for isotopic impurities in the Spectrum Mill
747 protein/peptide summary module using the afRICA correction method which implements
748 determinant calculations according to Cramer's Rule and correction factors obtained from the
749 reagent manufacturer's certificate of analysis
750 (https://www.thermofisher.com/order/catalog/product/90406) for lot numbers VH310017. After
751 performing median-MAD normalization, a moderated two-sample t-test was applied to the
752 datasets to compare wild-type, *Grin2a*+/-, and *Grin2a*-/- sample groups at each age. A
753 comprehensive list of differentially abundant proteins for 3-month *Grin2a*+/- and *Grin2a*-/- cortical
754 synapse fraction samples is provided in Supplementary Table S6.

## Data and code availability

The datasets and codes used in our study will be made public upon publication of the manuscript.

## Acknowledgements

We thank S. McCarroll for providing valuable insights into data interpretation, Z. Tang and K. Maher for assistance on computational analysis, and J. Tian, S. Furniss, and C. Mehaffey for suggestions on manuscript writing. X.W. acknowledges the support from Stanley Center for Psychiatric Research at Broad Institute, Packard Fellowship for Science and Engineering, Merkin Institute Fellowship, National Institutes of Health (NIH) DP2 New Innovator Award (1DP2GM146245) and NIH BRAIN CONNECTS (UM1 NS132173). W.X.W. is a Damon Runyon–National Mah Jongg League Fellow, supported by the Damon Runyon Cancer Research Foundation (DRG no. 2512-23).

## Author information

These authors contributed equally: Mingrui Wu, Jiahao Huang

Contributions: M.W. designed and performed STARmap and RIBOmap experiments. J.H. performed downstream imaging data processing. J.H. and M.W. performed computational analysis. S.A., K.B., M.Y., B.D., H.K., and S.A.C. performed synaptic proteome profiling. I.P. and Y.Z. prepared mouse brain samples. H.C. prepared STARmap and RIBOmap probes. Z.F., S.L., and W.X.W. offered inputs on data analysis and interpretation. All authors contributed to writing and revising the manuscript and approved the final version. X.W. and M.S. conceptualized and supervised the project.

Corresponding authors: Xiao Wang (wangxiao@broadinstitute.org), Morgan Sheng (msheng@broadinstitute.org)

## Competing interests

X.W. is a scientific cofounder and consultant of Stellaromics and Convergence Bio. M.S. is SAB member and/or consultant of Neumora, Biogen, Illimis, CurieBio, Astex. Other authors declare no competing interests.

## Reference

1. Kahn, R. S. *et al.* Schizophrenia. *Nat. Rev. Dis. Primer* **1**, 15067 (2015).
2. Schizophrenia Working Group of the Psychiatric Genomics Consortium. Biological insights from 108 schizophrenia-associated genetic loci. *Nature* **511**, 421–427 (2014).

786 3. Singh, T. *et al.* Rare coding variants in ten genes confer substantial risk for
787 schizophrenia. *Nature* **604**, 509–516 (2022).
788 4. Wang, X. *et al.* Three-dimensional intact-tissue sequencing of single-cell transcriptional
789 states. *Science* **361**, (2018).
790 5. Zeng, H. *et al.* Spatially resolved single-cell translatomics at molecular resolution.
791 *Science* **380**, (2023).
792 6. Jauhar, S., Johnstone, M. & McKenna, P. J. Schizophrenia. *The Lancet* **399**, 473–486
793 (2022).
794 7. Moreno-Küstner, B., Martín, C. & Pastor, L. Prevalence of psychotic disorders and its
795 association with methodological issues. A systematic review and meta-analyses. *PLOS ONE*
796 **13**, e0195687 (2018).
797 8. Liddle, P. F. The Symptoms of Chronic Schizophrenia: A Re-examination of the Positive-
798 Negative Dichotomy. *Br. J. Psychiatry* **151**, 145–151 (1987).
799 9. Cardno, A. G. & Gottesman, I. I. Twin studies of schizophrenia: From bow-and-arrow
800 concordances to Star Wars Mx and functional genomics. *Am. J. Med. Genet.* **97**, 12–17
801 (2000).
802 10. Sullivan, P. F., Kendler, K. S. & Neale, M. C. Schizophrenia as a Complex Trait:
803 Evidence From a Meta-analysis of Twin Studies. *Arch. Gen. Psychiatry* **60**, 1187 (2003).
804 11. Owen, M. J., Sawa, A. & Mortensen, P. B. Schizophrenia. *The Lancet* **388**, 86–97
805 (2016).
806 12. Trubetskoy, V. *et al.* Mapping genomic loci implicates genes and synaptic biology in
807 schizophrenia. *Nature* **604**, 502–508 (2022).
808 13. Farsi, Z. & Sheng, M. Molecular mechanisms of schizophrenia: Insights from human
809 genetics. *Curr. Opin. Neurobiol.* **81**, 102731 (2023).
810 14. Harrison, P. J. & Bannerman, D. M. GRIN2A (NR2A): a gene contributing to
811 glutamatergic involvement in schizophrenia. *Mol. Psychiatry* **28**, 3568–3572 (2023).

812 15. Hu, W., MacDonald, M. L., Elswick, D. E. & Sweet, R. A. The glutamate hypothesis of
813 schizophrenia: evidence from human brain tissue studies. *Ann. N. Y. Acad. Sci.* **1338**, 38–57
814 (2015).
815 16. Kruse, A. O. & Bustillo, J. R. Glutamatergic dysfunction in Schizophrenia. *Transl.*
816 *Psychiatry* **12**, 500 (2022).
817 17. Moghaddam, B. & Javitt, D. From Revolution to Evolution: The Glutamate Hypothesis of
818 Schizophrenia and its Implication for Treatment. *Neuropsychopharmacology* **37**, 4–15 (2012).
819 18. Herzog, L. E. *et al.* Mouse mutants in schizophrenia risk genes GRIN2A and AKAP11
820 show EEG abnormalities in common with schizophrenia patients. *Transl. Psychiatry* **13**,
821 (2023).
822 19. Farsi, Z. *et al.* Brain-region-specific changes in neurons and glia and dysregulation of
823 dopamine signaling in Grin2a mutant mice. *Neuron* **111**, 3378-3396.e9 (2023).
824 20. Zhang, S. *et al.* Insights Into Translatomics in the Nervous System. *Front. Genet.* **11**,
825 599548 (2020).
826 21. Wang, Y., Yan, Y., Zhou, B. & Lin, M. Post-transcriptional dysregulation in autism,
827 schizophrenia, and bipolar disorder. *J. Biomed. Res.* **39**, 325 (2025).
828 22. Askenazi, M. *et al.* Compilation of reported protein changes in the brain in Alzheimer's
829 disease. *Nat. Commun.* **14**, 4466 (2023).
830 23. English, J. A. *et al.* Reduced protein synthesis in schizophrenia patient-derived olfactory
831 cells. *Transl. Psychiatry* **5**, e663–e663 (2015).
832 24. Laguesse, S. & Ron, D. Protein Translation and Psychiatric Disorders. *The*
833 *Neuroscientist* **26**, 21–42 (2020).
834 25. Shi, H. *et al.* Spatial atlas of the mouse central nervous system at molecular resolution.
835 *Nature* **622**, 552–561 (2023).
836 26. Owen, M. J., Sawa, A. & Mortensen, P. B. Schizophrenia. *The Lancet* **388**, 86–97
837 (2016).

838 27. Herbener, E. S. Emotional Memory in Schizophrenia. *Schizophr. Bull.* **34**, 875–887
839 (2008).
840 28. Lisman, J. E. *et al.* Circuit-based framework for understanding neurotransmitter and risk
841 gene interactions in schizophrenia. *Trends Neurosci.* **31**, 234–242 (2008).
842 29. Maher, K. *et al.* Mitigating autocorrelation during spatially resolved transcriptomics data
843 analysis. Preprint at https://doi.org/10.1101/2023.06.30.547258 (2023).
844 30. Ferrarelli, F. & Tononi, G. The Thalamic Reticular Nucleus and Schizophrenia.
845 *Schizophr. Bull.* **37**, 306–315 (2011).
846 31. Steullet, P. *et al.* The thalamic reticular nucleus in schizophrenia and bipolar disorder:
847 role of parvalbumin-expressing neuron networks and oxidative stress. *Mol. Psychiatry* **23**,
848 2057–2065 (2018).
849 32. Kotliar, D. *et al.* Identifying gene expression programs of cell-type identity and cellular
850 activity with single-cell RNA-Seq. *eLife* **8**, e43803 (2019).
851 33. Fang, Z., Liu, X. & Peltz, G. GSEApy: a comprehensive package for performing gene set
852 enrichment analysis in Python. *Bioinformatics* **39**, btac757 (2023).
853 34. Vieira, M., Yong, X. L. H., Roche, K. W. & Anggono, V. Regulation of NMDA glutamate
854 receptor functions by the GluN2 subunits. *J. Neurochem.* **154**, 121–143 (2020).
855 35. Hardingham, G. E. & Bading, H. Synaptic versus extrasynaptic NMDA receptor
856 signalling: implications for neurodegenerative disorders. *Nat. Rev. Neurosci.* **11**, 682–696
857 (2010).
858 36. Lewis, D. A., Curley, A. A., Glausier, J. R. & Volk, D. W. Cortical parvalbumin
859 interneurons and cognitive dysfunction in schizophrenia. *Trends Neurosci.* **35**, 57–67 (2012).
860 37. Schmidt, M. J. & Mirnics, K. Neurodevelopment, GABA System Dysfunction, and
861 Schizophrenia. *Neuropsychopharmacology* **40**, 190–206 (2015).
862 38. Lewis, D. A. Inhibitory neurons in human cortical circuits: substrate for cognitive
863 dysfunction in schizophrenia. *Curr. Opin. Neurobiol.* **26**, 22–26 (2014).

864 39. Akbarian, S. & Huang, H.-S. Molecular and cellular mechanisms of altered
865 GAD1/GAD67 expression in schizophrenia and related disorders. *Brain Res. Rev.* **52**, 293–
866 304 (2006).
867 40. Volk, D. W. *et al.* Deficits in Transcriptional Regulators of Cortical Parvalbumin Neurons
868 in Schizophrenia. *Am. J. Psychiatry* **169**, 1082–1091 (2012).
869 41. Pan, Z. Z. Transcriptional control of *Gad2*. *Transcription* **3**, 68–72 (2012).
870 42. Sun, Y. *et al.* Gamma oscillations in schizophrenia: Mechanisms and clinical
871 significance. *Brain Res.* **1413**, 98–114 (2011).
872 43. Chen, Z., Wimmer, R. D., Wilson, M. A. & Halassa, M. M. Thalamic Circuit Mechanisms
873 Link Sensory Processing in Sleep and Attention. *Front. Neural Circuits* **9**, (2016).
874 44. Beneyto, M., Abbott, A., Hashimoto, T. & Lewis, D. A. Lamina-Specific Alterations in
875 Cortical GABAA Receptor Subunit Expression in Schizophrenia. *Cereb. Cortex* **21**, 999–1011
876 (2011).
877 45. Asiedu, M. N., Mejia, G. L., Hübner, C. A., Kaila, K. & Price, T. J. Inhibition of Carbonic
878 Anhydrase Augments GABAA Receptor-Mediated Analgesia via a Spinal Mechanism of
879 Action. *J. Pain* **15**, 395–406 (2014).
880 46. Ruusuvuori, E. *et al.* Neuronal carbonic anhydrase VII provides GABAergic excitatory
881 drive to exacerbate febrile seizures. *EMBO J.* **32**, 2275–2286 (2013).
882 47. Kreitzer, A. C. & Malenka, R. C. Striatal Plasticity and Basal Ganglia Circuit Function.
883 *Neuron* **60**, 543–554 (2008).
884 48. Lee, H. J. *et al.* Activation of Direct and Indirect Pathway Medium Spiny Neurons Drives
885 Distinct Brain-wide Responses. *Neuron* **91**, 412–424 (2016).
886 49. Gerfen, C. R. Segregation of D1 and D2 dopamine receptors in the striatal direct and
887 indirect pathways: An historical perspective. *Front. Synaptic Neurosci.* **14**, 1002960 (2023).
888 50. Tyssowski, K. M. *et al.* Different Neuronal Activity Patterns Induce Different Gene
889 Expression Programs. *Neuron* **98**, 530-546.e11 (2018).

890 51. Song, L., Chen, W., Hou, J., Guo, M. & Yang, J. Spatially resolved mapping of cells
891 associated with human complex traits. *Nature* **641**, 932–941 (2025).
892 52. Najjar, S. *et al.* Neurovascular Unit Dysfunction and Blood–Brain Barrier
893 Hyperpermeability Contribute to Schizophrenia Neurobiology: A Theoretical Integration of
894 Clinical and Experimental Evidence. *Front. Psychiatry* **8**, 83 (2017).
895 53. Theparambil, S. M. *et al.* Astrocytes regulate brain extracellular pH via a neuronal
896 activity-dependent bicarbonate shuttle. *Nat. Commun.* **11**, 5073 (2020).
897 54. Pfrieger, F. W. & Ungerer, N. Cholesterol metabolism in neurons and astrocytes. *Prog.*
898 *Lipid Res.* **50**, 357–371 (2011).
899 55. Ferris, H. A. *et al.* Loss of astrocyte cholesterol synthesis disrupts neuronal function and
900 alters whole-body metabolism. *Proc. Natl. Acad. Sci.* **114**, 1189–1194 (2017).
901 56. Gjervan, S. C., Ozgoren, O. K., Gow, A., Stockler-Ipsiroglu, S. & Pouladi, M. A. Claudin-
902 11 in health and disease: implications for myelin disorders, hearing, and fertility. *Front. Cell.*
903 *Neurosci.* **17**, 1344090 (2024).
904 57. Butovsky, O. & Weiner, H. L. Microglial signatures and their role in health and disease.
905 *Nat. Rev. Neurosci.* **19**, 622–635 (2018).
906 58. Lyu, M. *et al.* Tnfrsf12a-Mediated Atherosclerosis Signaling and Inflammatory Response
907 as a Common Protection Mechanism of Shuxuening Injection Against Both Myocardial and
908 Cerebral Ischemia-Reperfusion Injuries. *Front. Pharmacol.* **9**, 312 (2018).
909 59. Kimura, S., Lok, J., Gelman, I. H., Lo, E. H. & Arai, K. Role of A-Kinase Anchoring
910 Protein 12 in the Central Nervous System. *J. Clin. Neurol.* **19**, 329 (2023).
911 60. Bereshchenko, O., Migliorati, G., Bruscoli, S. & Riccardi, C. Glucocorticoid-Induced
912 Leucine Zipper: A Novel Anti-inflammatory Molecule. *Front. Pharmacol.* **10**, 308 (2019).
913 61. Ling, E. *et al.* A concerted neuron–astrocyte program declines in ageing and
914 schizophrenia. *Nature* **627**, 604–611 (2024).

915 62. Wylie, K. P. & Tregellas, J. R. The role of the insula in schizophrenia. *Schizophr. Res.*
916 **123**, 93–104 (2010).
917 63. Haydon, P. G. & Carmignoto, G. Astrocyte Control of Synaptic Transmission and
918 Neurovascular Coupling. *Physiol. Rev.* **86**, 1009–1031 (2006).
919 64. Khakh, B. S. On astrocyte-neuron interactions: Broad insights from the striatum. *Neuron*
920 **113**, 3079–3107 (2025).
921 65. Brown, L. S. *et al.* Pericytes and Neurovascular Function in the Healthy and Diseased
922 Brain. *Front. Cell. Neurosci.* **13**, (2019).
923 66. Hasel, P. *et al.* Neurons and neuronal activity control gene expression in astrocytes to
924 regulate their development and metabolism. *Nat. Commun.* **8**, 15132 (2017).
925 67. Grace, A. A. Dysregulation of the dopamine system in the pathophysiology of
926 schizophrenia and depression. *Nat. Rev. Neurosci.* **17**, 524–532 (2016).
927 68. Aryal, S. *et al.* Deep proteomics identifies shared molecular pathway alterations in
928 synapses of patients with schizophrenia and bipolar disorder and mouse model. *Cell Rep.* **42**,
929 112497 (2023).
930 69. Matosin, N. *et al.* Molecular evidence of synaptic pathology in the CA1 region in
931 schizophrenia. *Npj Schizophr.* **2**, 16022 (2016).
932 70. Dejanovic, B. *et al.* Changes in the Synaptic Proteome in Tauopathy and Rescue of Tau-
933 Induced Synapse Loss by C1q Antibodies. *Neuron* **100**, 1322-1336.e7 (2018).

934 **Figures**

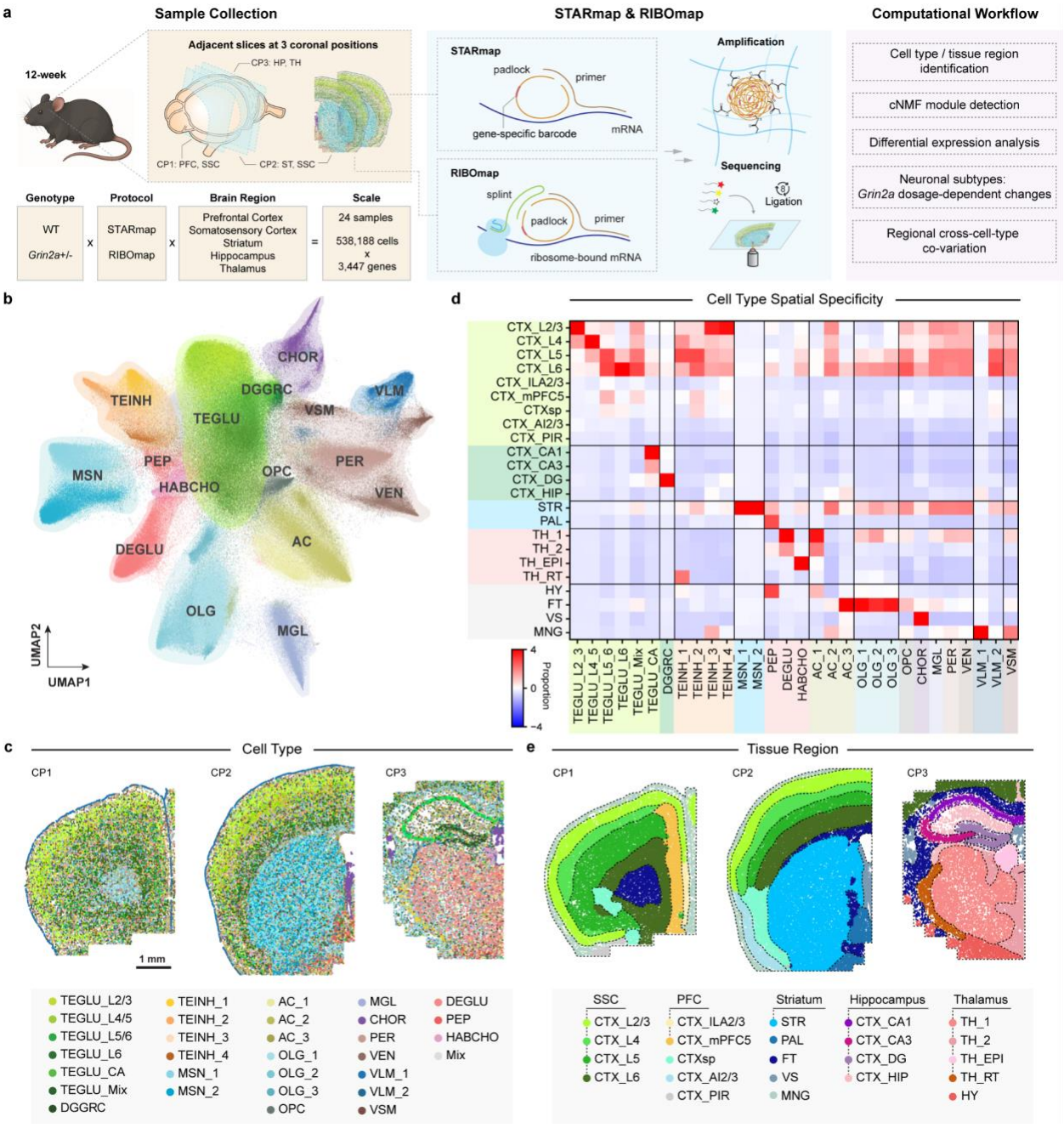


935

936 **Fig. 1: Integrative profiling of *Grin2a*+/- mouse brain.**

937 **a**, Research schematics. Mouse brain slices were collected from 12-week wild-type and *Grin2a*+/-
938 mice at three coronal positions, covering multiple brain regions of interest: prefrontal cortex (PFC),
939 somatosensory cortex (SSC), striatum (ST), hippocampus (HP), and thalamus (TH). RIBOmap
940 and STARmap targeting 3,447 genes were performed on each pair of adjacent slices,
941 respectively. Computational workflow included cell type classification, tissue region identification,
942 differential expression (DE) analysis, and cross-cell-type co-variation analysis. **b**, Uniform

943 Manifold Approximation and Projection (UMAP) of 538,188 cells colored by detailed subtypes and
944 labeled with top-level major cell types: AC, astrocytes; CHOR, choroid plexus epithelial cells;
945 DEGLU, diencephalon excitatory neurons; DGGRC, dentate gyrus granule cells; HABCHO,
946 habenula cholinergic neurons; MGL, microglia; MSN, medium spiny neurons; OLG,
947 oligodendrocytes; OPC, oligodendrocyte precursor cells; PEP, peptidergic neurons; PER,
948 pericytes; TEGLU, telencephalon projecting excitatory neurons; TEINH, telencephalon inhibitory
949 interneurons; VEN, vascular endothelial cells; VLM, vascular and leptomeningeal cells; VSM,
950 vascular smooth muscle cells. **c**, Spatial visualizations showing subtypes distribution at 3 coronal
951 positions. **d**, Heatmap showing cell subtype compositions across molecular tissue regions. The
952 proportion of each cell subtype is calculated for every molecular tissue region. Then, the z-scores
953 of these percentages are plotted for each cell type, with subtypes grouped under their respective
954 top-level cell types. CTX, Cerebral cortex; ILA, Infralimbic area; CTXsp, Cortical subplate; AI,
955 Agranular insular area; PIR, Piriform area; HIP, Hippocampal region; CA, Ammon's horn; DG,
956 Dentate gyrus; STR, Striatum; PAL, Pallidum; TH, Thalamus; EPI, Epithalamus; RT, Reticular
957 nucleus; HY, Hypothalamus; FT, Fibre tracts; VS, Ventricular systems; MNG, Meninges. **e**, Spatial
958 visualizations showing the delineation of molecular tissue regions by SPIN at 3 coronal positions.

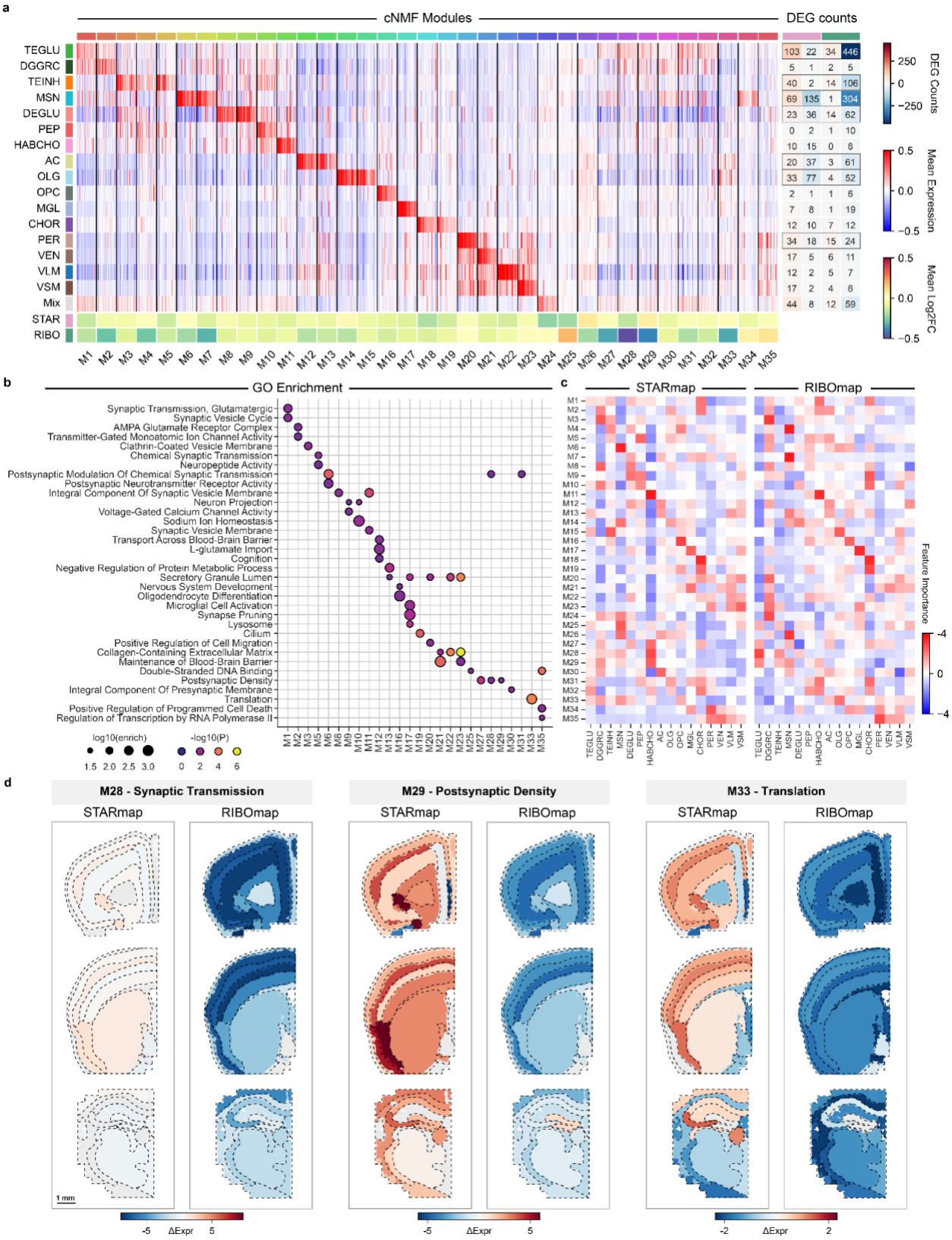
a
cNMF Modules
DEG counts
TEGLU
DGGRC
TEINH
MSN
DEGLU
PEP
HABCHO
AC
OLG
OPC
MGL
CHOR
PER
VEN
VLM
VSM
Mix
STAR
RIBO
DEG Counts
Mean Expression
Mean Log2FC
b
GO Enrichment
Synaptic Transmission, Glutamatergic
Synaptic Vesicle Cycle
AMPA Glutamate Receptor Complex
Transmitter-Gated Monoatomic Ion Channel Activity
Clathrin-Coated Vesicle Membrane
Chemical Synaptic Transmission
Neuropeptide Activity
Postsynaptic Modulation Of Chemical Synaptic Transmission
Postsynaptic Neurotransmitter Receptor Activity
Integral Component Of Synaptic Vesicle Membrane
Neuron Projection
Voltage-Gated Calcium Channel Activity
Sodium Ion Homeostasis
Synaptic Vesicle Membrane
Transport Across Blood-Brain Barrier
L-glutamate Import
Cognition
Negative Regulation of Protein Metabolic Process
Secretory Granule Lumen
Nervous System Development
Oligodendrocyte Differentiation
Microglial Cell Activation
Synapse Pruning
Lysosome
Cilium
Positive Regulation of Cell Migration
Collagen-Containing Extracellular Matrix
Maintenance of Blood-Brain Barrier
Double-Stranded DNA Binding
Postsynaptic Density
Integral Component Of Presynaptic Membrane
Translation
Positive Regulation of Programmed Cell Death
Regulation of Transcription by RNA Polymerase II
log10(enrich)
-log10(P)
c
STARmap
RIBOmap
Feature Importance
d
M28 - Synaptic Transmission
M29 - Postsynaptic Density
M33 - Translation
STARmap
RIBOmap
1 mm
ΔExpr

960 **Fig. 2: System-level analysis of gene expression modules in transcriptome and**
961 **translatome.**

962 **a**, Gene expression module identification with cNMF in spatial transcriptome and translatome.
963 Multi-panel heatmap showing 35 detected gene modules: Expression of top 50 genes with the
964 highest loading of each module in major cell types (main), cell-type-specific DEG count (right),
965 and averaged log fold-change in STARmap and RIBOmap of top-50 genes from each module in
966 the total cell population (bottom). Cell types showing prominent changes were outlined in black.
967 **b**, GO enrichment analysis of cNMF modules with the top 50 genes; Color scale, negative log-
968 transformed adjusted p-value; dot size, log-transformed enrichment score. **c**, Heatmap displaying
969 module importance for predicting genotypes across major cell types in STARmap (left) and
970 RIBOmap (right). A Random Forest classifier was trained using aggregated module expression
971 to distinguish WT from *Grin2a*+/− cells. **d**, Spatial visualizations of differential expression of
972 module M28, M29, and M33 in STARmap (left) and RIBOmap (right).

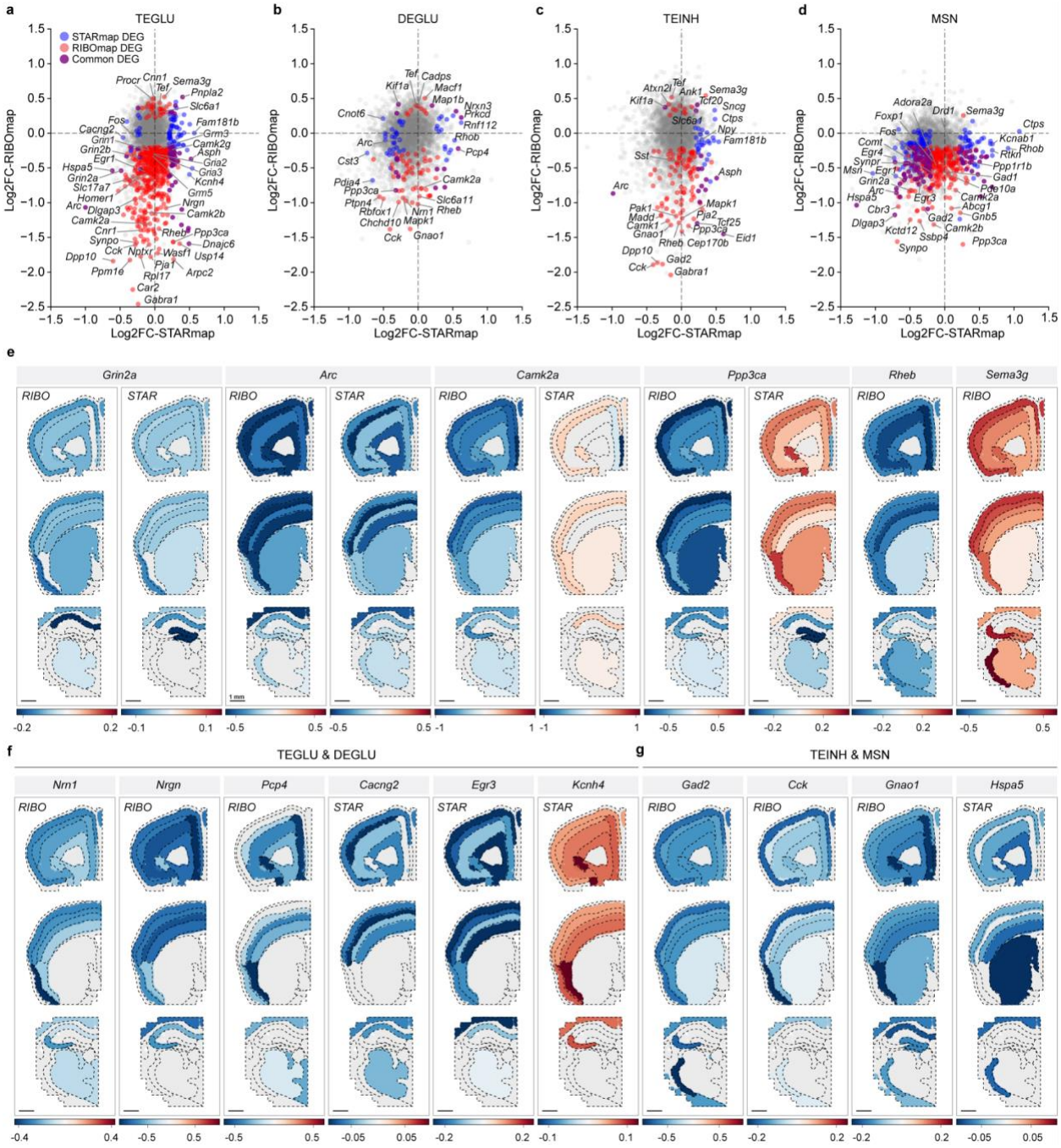


**Fig. 3: *Grin2a* LoF triggers distinct molecular responses in major neuronal populations.**

**a-d**, STARmap vs. RIBOmap log fold-change plots of 4 neuronal cell types of interest: TEGLU (**a**), DEGLU (**b**), TEINH (**c**), and MSN (**d**). DEGs with significant (adjusted p-value < 0.05, |Log2FC| ≥ 0.2) log fold-change in STARmap only, RIBOmap only, and both modalities are colored in blue, red, and purple, respectively. **e,** Spatial visualizations of representative differentially expressed genes in four neuronal populations of interest. **f, g**, Spatial visualizations

980 of differentially expressed genes for excitatory neurons TEGLU and DEGLU (**f**) and inhibitory
981 neurons TEINH and MSN (**g**) identified in STARmap and RIBOmap. Regional log-fold changes
982 were calculated for the neuronal populations shown in each panel.

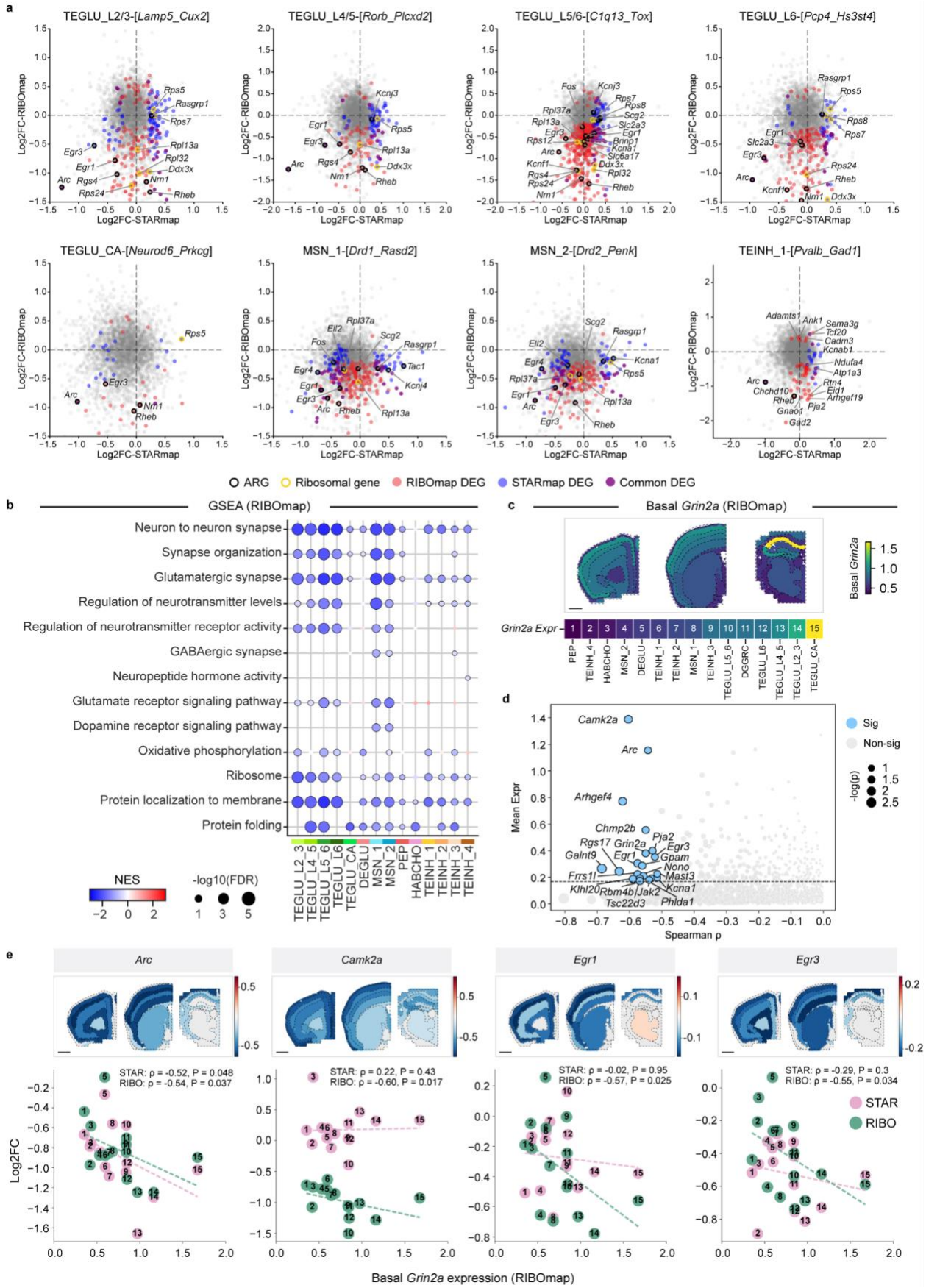
a
TEGLU_L2/3-[Lamp5_Cux2]
TEGLU_L4/5-[Rorb_Plcxd2]
TEGLU_L5/6-[C1q13_Tox]
TEGLU_L6-[Pcp4_Hs3st4]
TEGLU_CA-[Neurod6_Prkcg]
MSN_1-[Drd1_Rasd2]
MSN_2-[Drd2_Penk]
TEINH_1-[Pvalb_Gad1]
Log2FC-RIBOmap
Log2FC-STARmap
ARG
Ribosomal gene
RIBOmap DEG
STARmap DEG
Common DEG
b
GSEA (RIBOmap)
Neuron to neuron synapse
Synapse organization
Glutamatergic synapse
Regulation of neurotransmitter levels
Regulation of neurotransmitter receptor activity
GABAergic synapse
Neuropeptide hormone activity
Glutamate receptor signaling pathway
Dopamine receptor signaling pathway
Oxidative phosphorylation
Ribosome
Protein localization to membrane
Protein folding
TEGLU_L2_3
TEGLU_L4_5
TEGLU_L5_6
TEGLU_L6
TEGLU_CA
DEGLU
MSN_1
MSN_2
PEP
HABCHO
TEINH_1
TEINH_2
TEINH_3
TEINH_4
NES
-log10(FDR)
c
Basal Grin2a (RIBOmap)
Basal Grin2a
Grin2a Expr
d
Camk2a
Arc
Arhgef4
Chmp2b
Rgs17
Grin2a
Pja2
Egr3
Galnt9
Egr1
Gpam
Nono
Frrs1l
Mast3
Klhl20
Rbm4b
Jak2
Kcna1
Tsc22d3
Phlda1
Sig
Non-sig
-log(p)
Mean Expr
Spearman ρ
e
Arc
Camk2a
Egr1
Egr3
STAR: ρ = -0.52, P = 0.048
RIBO: ρ = -0.54, P = 0.037
STAR: ρ = 0.22, P = 0.43
RIBO: ρ = -0.60, P = 0.017
STAR: ρ = -0.02, P = 0.95
RIBO: ρ = -0.57, P = 0.025
STAR: ρ = -0.29, P = 0.3
RIBO: ρ = -0.55, P = 0.034
STAR
RIBO
Log2FC
Basal Grin2a expression (RIBOmap)

983

984 **Fig. 4: Intrinsic *Grin2a* expression predicts vulnerability to LoF across neuronal subtypes**

985 **a**, STARmap vs. RIBOmap log fold-change plots of neuronal subtypes of interest: TEGLU_L2/3,
986 TEGLU_L4/5, TEGLU_L5/6, TEGLU_L6, TEGLU_CA, MSN_1, MSN_2, and TEINH_1. DEGs
987 with significant (adjusted p-value < 0.05, Log2FC ≥ 0.2) log fold-change in STARmap only,
988 RIBOmap only, and both modalities are colored in blue, red, and purple, respectively. Activity-
989 regulated genes (ARGs) and ribosomal genes identified as DEGs were highlighted with black and
990 yellow circles, respectively. **b**, Gene set enrichment analysis (GSEA) of DEGs identified for
991 neuronal subtypes in RIBOmap. Color scale, normalized enrichment score (NES); dot size,
992 negative log-transformed FDR q-value. **c**, Spatial map of RIBOmap basal *Grin2a* expression (top)
993 and ranking of neuronal subtypes based on RIBOmap basal *Grin2a* expression (bottom). **d**,
994 Scatter plot showing genes with negative Spearman's ρ between basal *Grin2a* expression and
995 RIBOmap log fold-change across neuronal subtypes. Genes with a p-value lower than 0.05 and
996 passing the 75% expression percentile across neuronal subtypes were labeled. Dot size, negative
997 log-transformed p-value. **e**, Relationship between basal *Grin2a* expression levels and translation
998 reduction of example genes across neuronal subtypes (bottom) and spatially heterogeneous
999 translation reduction of these genes across tissue regions (top).

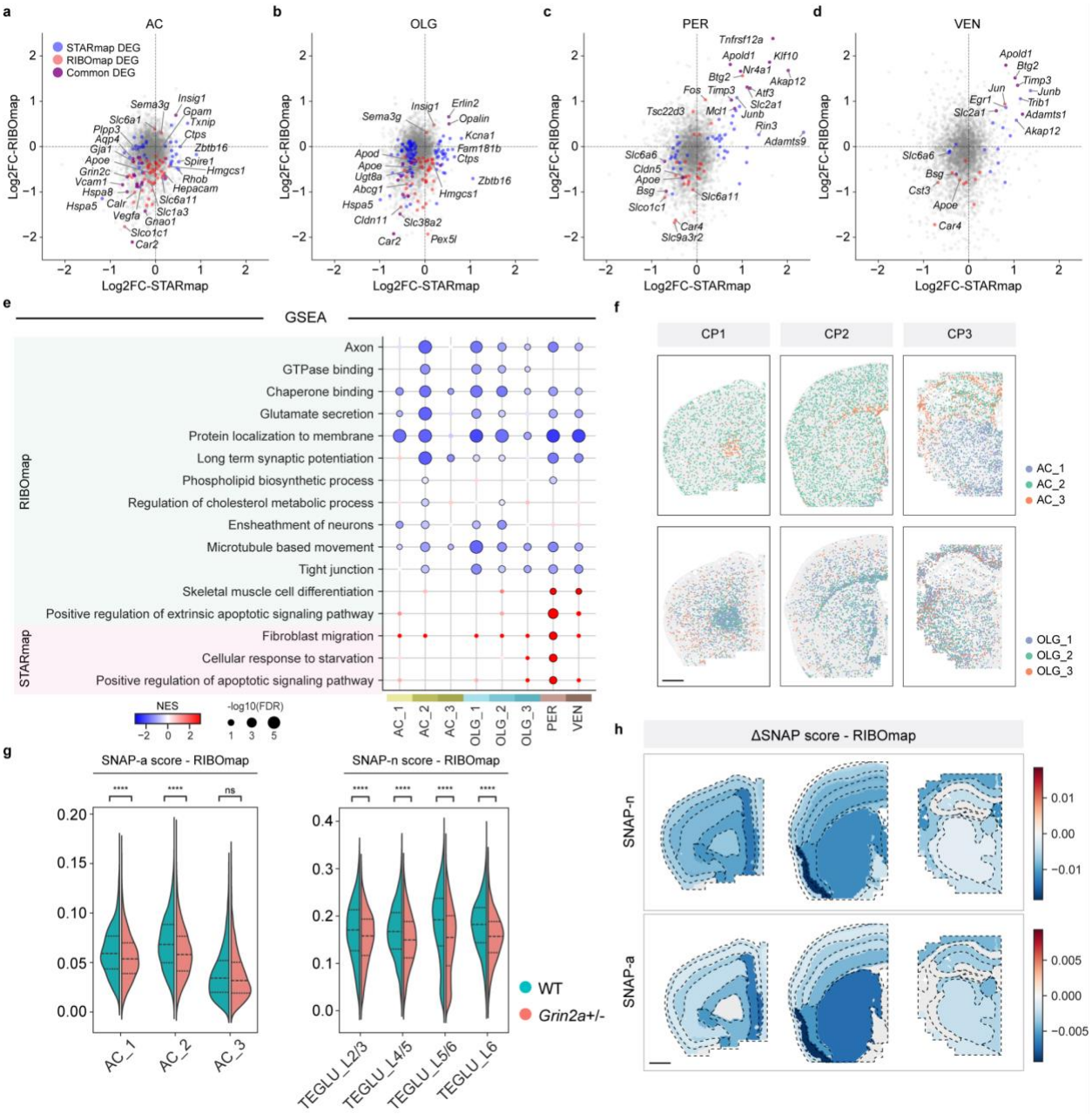


**Fig. 5: Transcriptional and translational changes in non-neuronal cell types.**

**a-d**, STARmap vs. RIBOmap log fold-change plots of astrocytes (AC), oligodendrocytes (OLG), pericytes (PER), and vascular endothelial cells (VEN). DEGs with significant (adjusted p-value < 0.05, |Log2FC| ≥ 0.2) log fold-change in STARmap only, RIBOmap only, and both modalities are colored in blue, red, and purple, respectively. **e**, GSEA of DEGs identified in astrocytes, oligodendrocytes, pericytes, and vascular endothelial cells. Color scale, normalized enrichment score (NES); dot size, negative log-transformed FDR q-value. **f**, Spatial visualizations showing the subtype distribution of astrocyte (top) and oligodendrocyte (bottom) at 3 coronal positions. Scale bar, 1 mm. **g**, Violin plots illustrating the difference between WT and *Grin2a*+/- in SNAP-a

1010 gene program scores in astrocyte subtypes (left) and SNAP-n gene program scores in cortical
1011 TEGLU subtypes (right) in RIBOmap. The P value was calculated using a two-sided independent
1012 t-test. ****P < 0.0001. **h**, Spatial visualizations of SNAP-n score difference in TEGLU cortical
1013 neurons (top) and SNAP-a score difference in astrocytes (bottom) in RIBOmap. Scale bar, 1 mm.

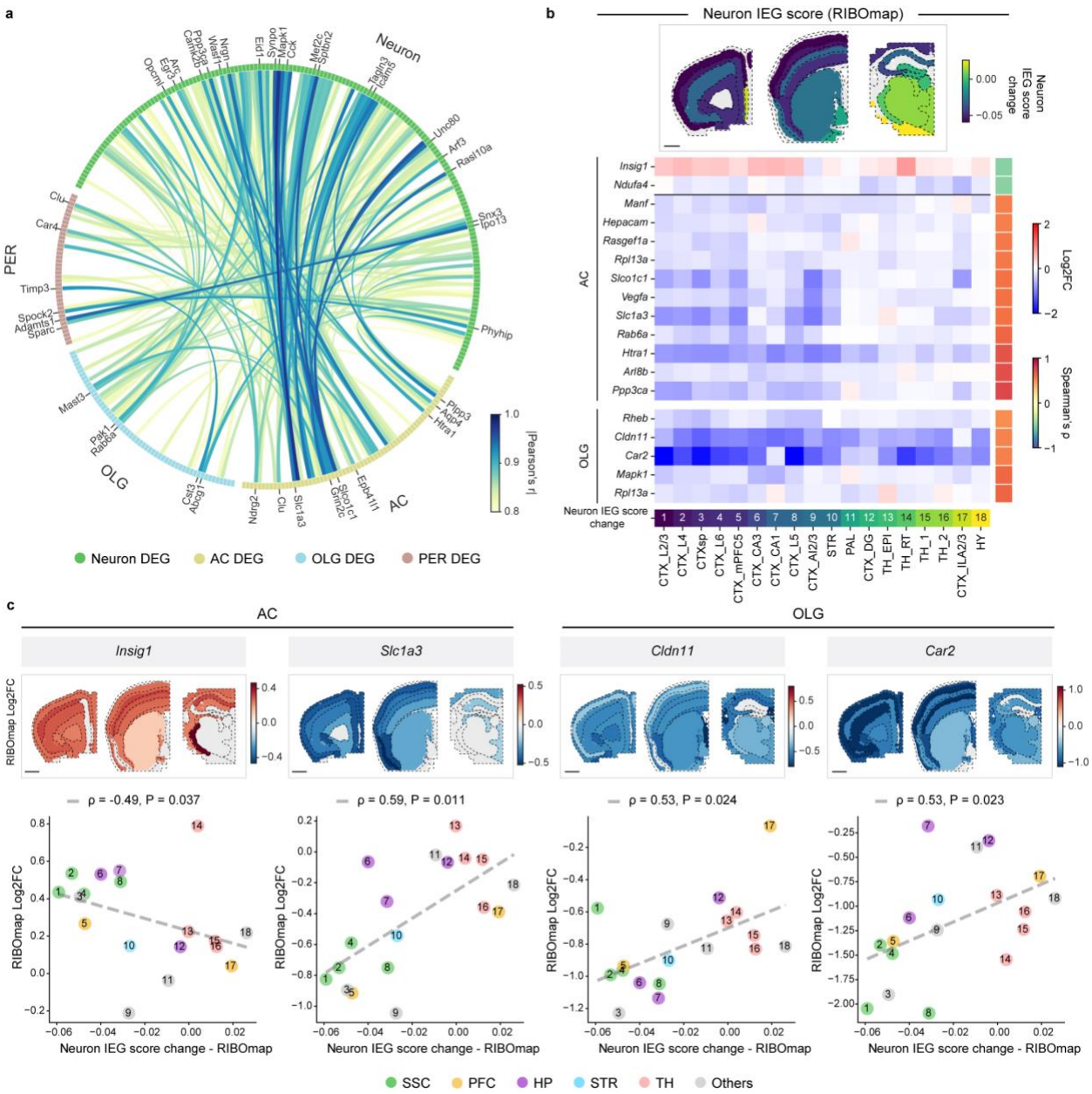


**Fig. 6: Translational co-variation among neuronal and non-neuronal cell types across brain regions.**

**a**, Chord diagram showing pairwise correlations of DEGs across neuron, astrocyte, oligodendrocyte, and pericyte based on region-specific RIBOmap log fold-change. Chord color, absolute value of pairwise Pearson's correlation coefficient r. **b**, Heatmap showing significant correlations between the regional log fold-change of glial DEGs from RIBOmap and changes in regional neuron RIBOmap IEG scores (bottom, p-value < 0.05), along with the spatial distribution of these IEG score changes (top). **c**, Relationship between regional neuron RIBOmap IEG score change and RIBOmap log fold-change of example glial DEGs (bottom), spatial heterogeneity of RIBOmap log fold-change of these genes across tissue regions (top).

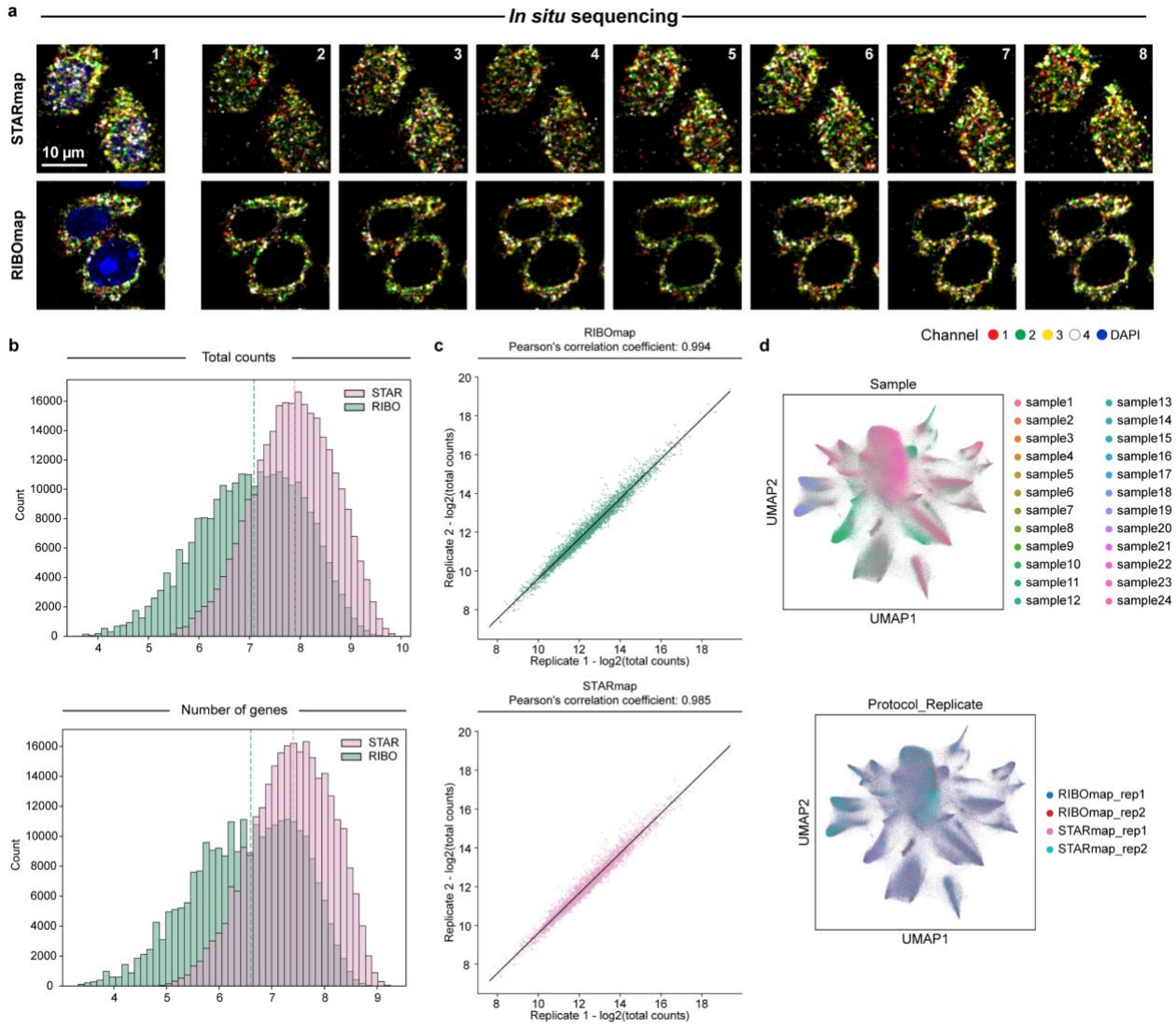


**Extended Data Fig. 1: Quality assessment of spatially resolved single-cell transcriptional and translational data.**

**a**, Representative images showing the sequential mapping of cDNA amplicons for STARmap (top) and RIBOmap (bottom) in mouse brain tissue sections. **b**, Histogram of the number of transcripts (top) and genes (bottom) in each cell after logarithmic transformation (log2) of STARmap and RIBOmap datasets. The median reads per cell are 237 for STARmap and 136 for RIBOmap, while the median genes per cell are 170 for STARmap and 97 for RIBOmap. **c**, The correlation of the number of reads for each gene between the two biological replicates in RIBOmap (top) and STARmap (bottom). **d**, UMAP showing the distribution of cells across 24 samples (top) and replicates in each modality (bottom).

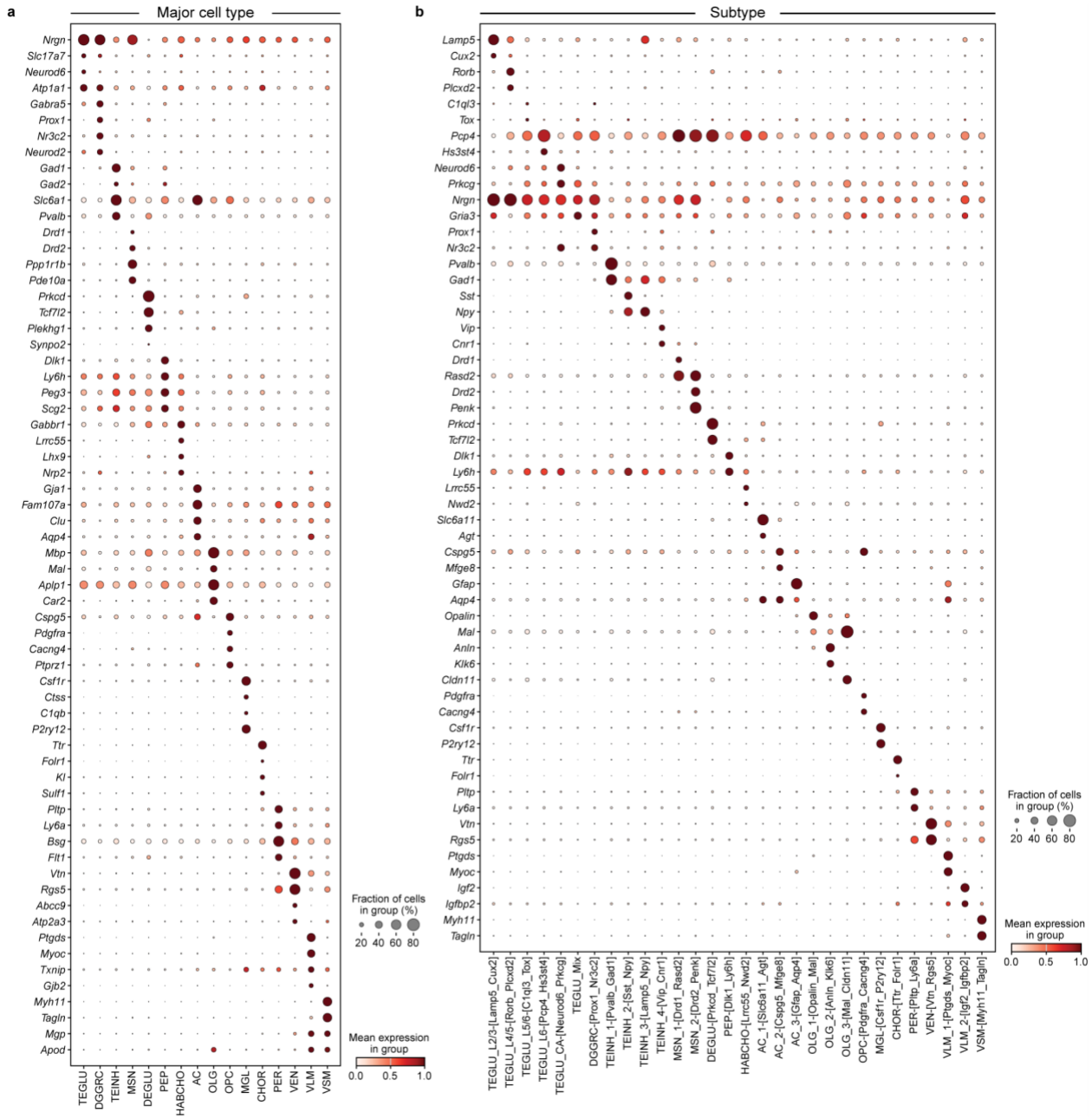


**Extended Data Fig. 2: Marker genes for major cell types and subtypes on the integrated dataset.**

**a**, Dot plot showing the expression level of representative markers across different major cell types. Color scale, averaged gene expression; dot size, the percentage of cells expressing the genes within each major cell type. **b**, Dot plot showing the expression level of representative markers across different subtypes. Color scale, averaged gene expression; dot size, the percentage of cells expressing the genes within each subtype.

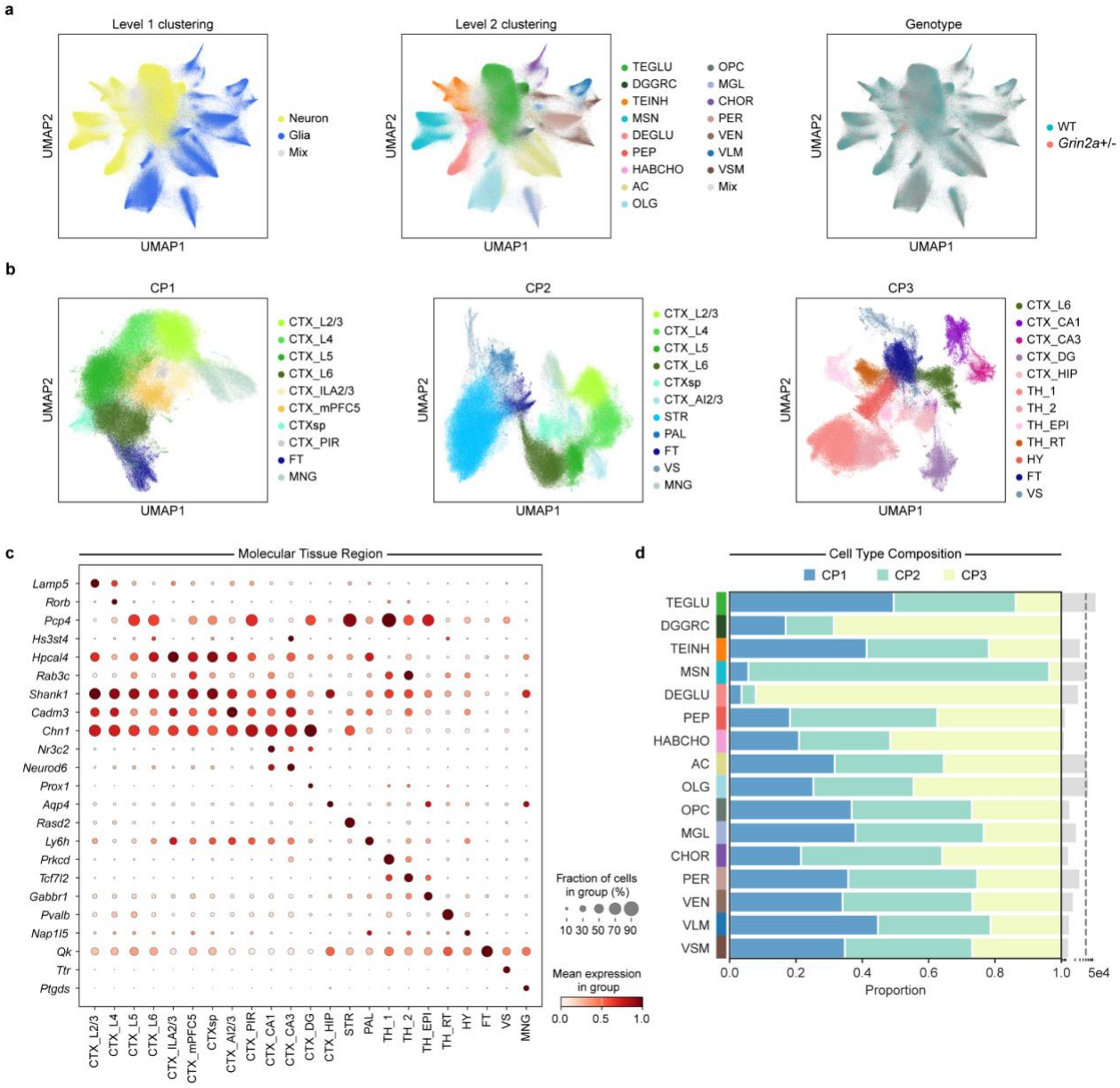


**Extended Data Fig. 3: Multi-level cell type classification and tissue region identification with SPIN**

**a**, UMAPs showing the distribution of cells colored by level 1 cell type annotations (left), level 2 cell type annotations (mid), and genotypes (right). **b**, UMAP of molecular tissue region annotation by SPIN at each coronal position. **c**, Dot plot showing the expression level of representative markers across molecular tissue regions. Color scale, averaged gene expression; dot size, the percentage of cells expressing the genes within each region. **d**, Bar plot showing major cell type composition at each coronal position.

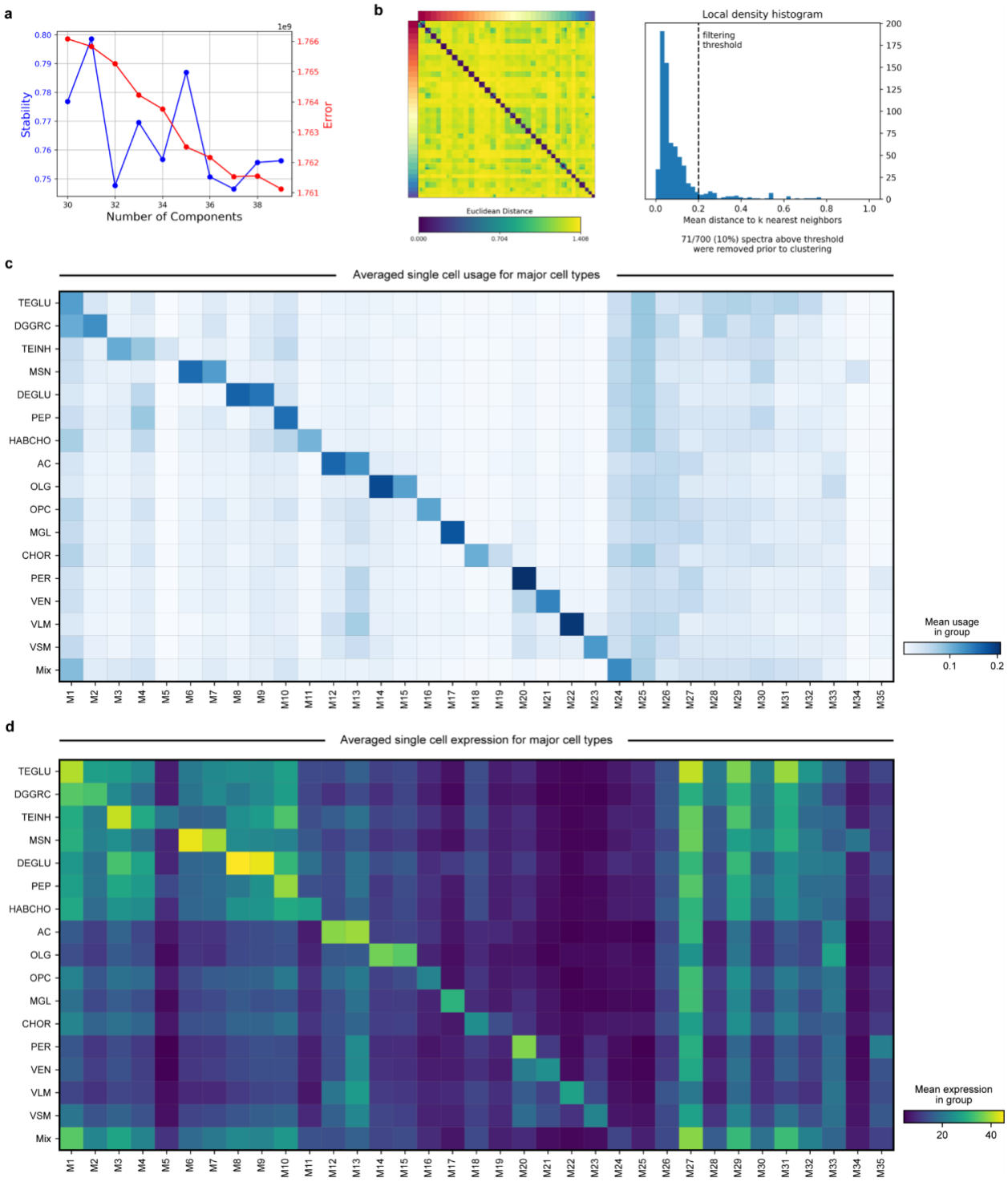


**Extended Data Fig. 4: Gene module identification with cNMF**

**a**, Visualization showing the tradeoff between error and stability of cNMF factors in relation to the number of factors k. 35 factors were requested based on these results. **b**, Clustermap showing the consensus matrix factorization estimates, with each color on the x- and y-axes representing

1058 one of the 35 cNMF factors. **c-d**, Matrix plot showing single cell usage score (**c**) and averaged
1059 gene expression (**d**) of each gene module across major cell types.

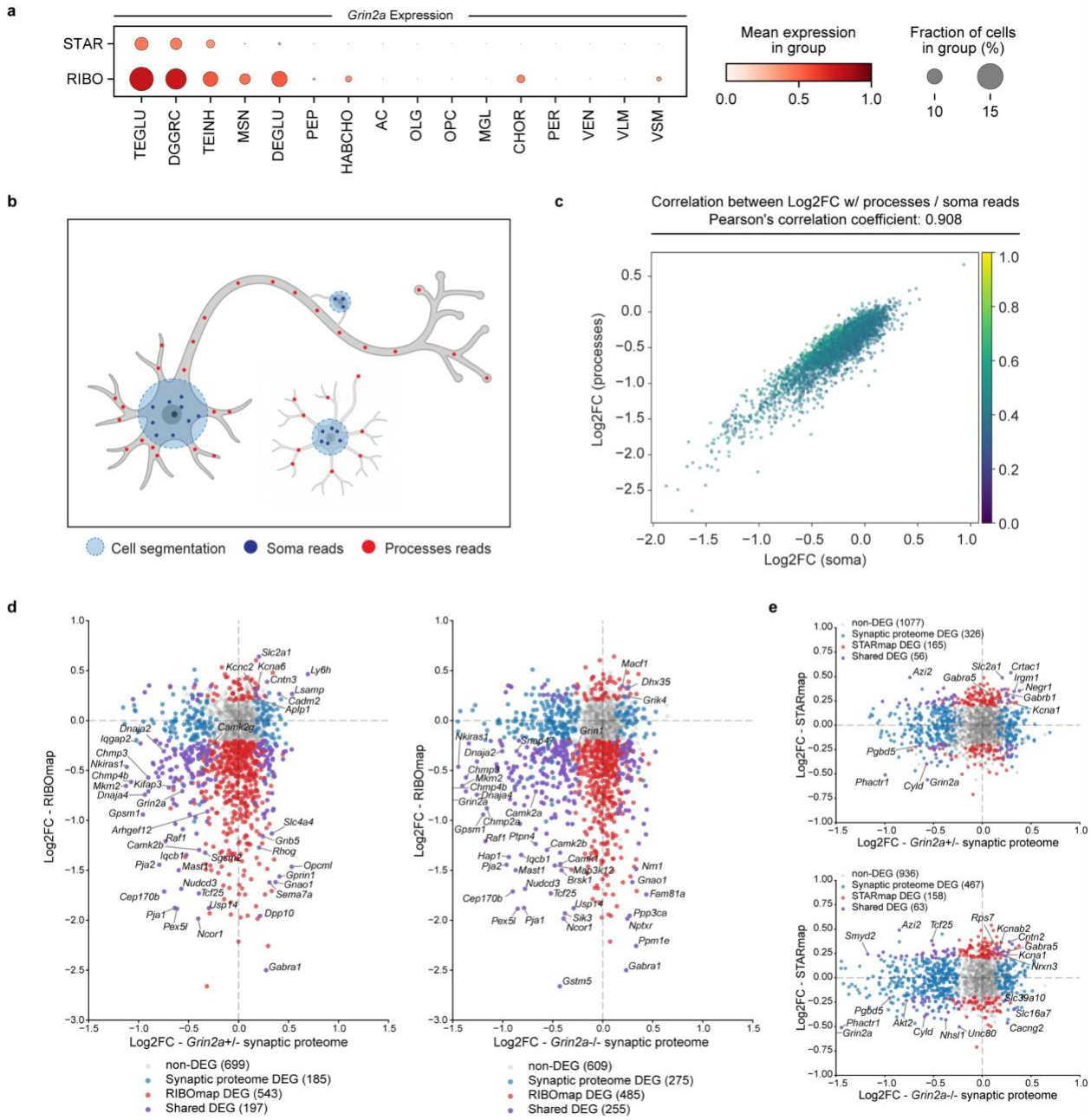


**Extended Data Fig. 5: Comparison between RIBOmap/STARmap and synaptic proteome.**

**a**, Dotplot showing the expression of *Grin2a* in major cell types measured by STARmap and RIBOmap. Color scale, averaged gene expression; Dot size, expression percentage. **b**, Schematics showing soma- vs. processes-reads at the single cell level. Signals outside the segmentation area were treated as reads in the neuronal processes. **c**, Scatter plot comparing the log fold-change values of each gene calculated from soma-reads versus process-reads. **d**, RIBOmap log fold-change vs. cortical synaptic proteome log fold-change in *Grin2a*+/- and *Grin2a*-/- mutants. **e**, STARmap log fold-change vs. cortical synaptic proteome log fold-change in *Grin2a*+/- and *Grin2a*-/- mutants.

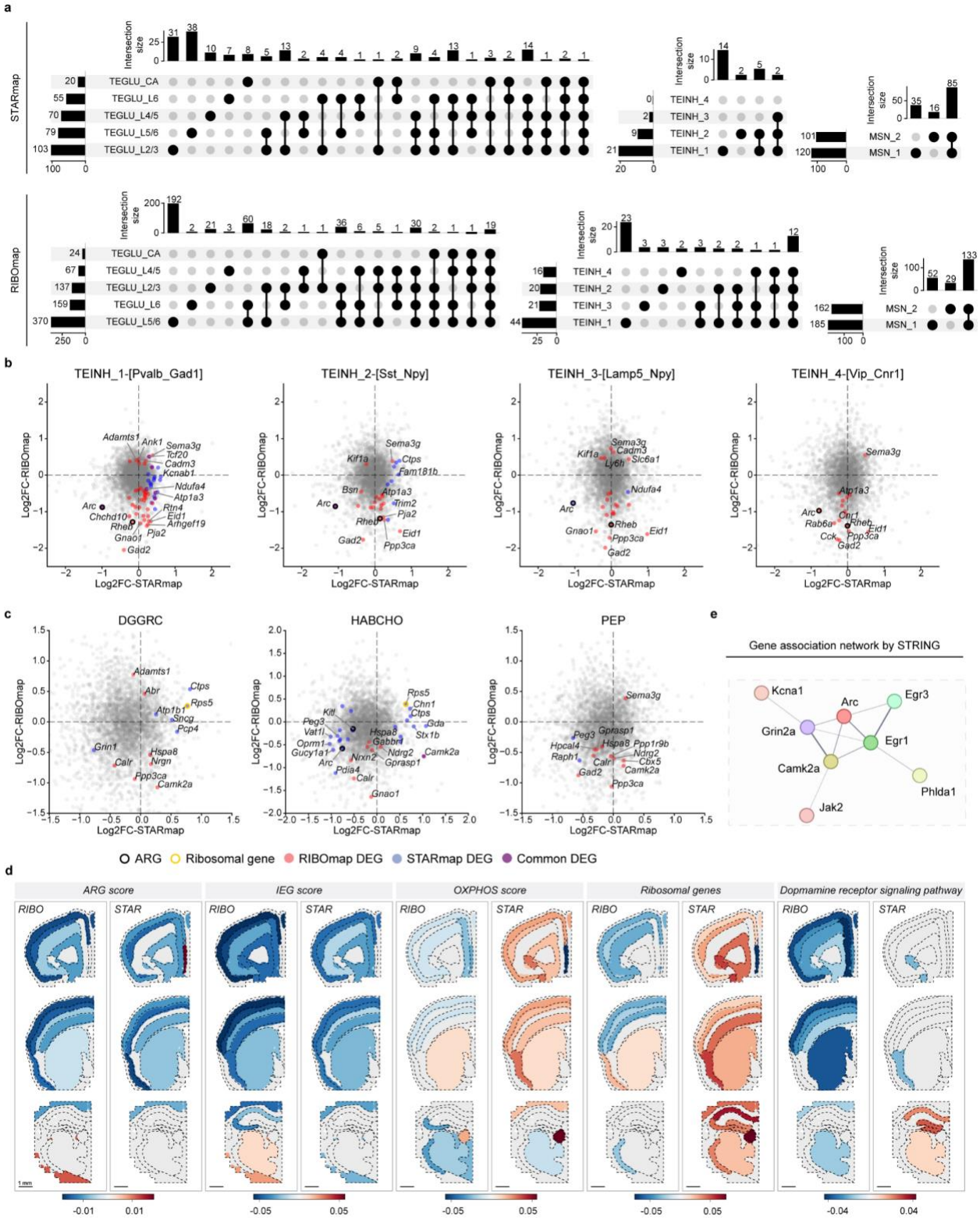


**Extended Data Fig. 6: Neuronal subtype DEG**

**a**, STARmap and RIBOmap DEG overlap between TEGLU, TEINH, and MSN subtypes. **b**, STARmap vs. RIBOmap log fold-change plot of 4 TEINH subtypes. **c**, STARmap vs. RIBOmap

1074 log fold-change plot of DGGRC, HABCHO, and PEP. **d**, Spatial visualizations of gene set score
1075 differences between two genotypes in STARmap and RIBOmap. Scale**e**, Pathway-level
1076 interactions among genes showing *Grin2a*-dependent translation reduction by the STRING
1077 interactome database. Edge width represents association confidence.

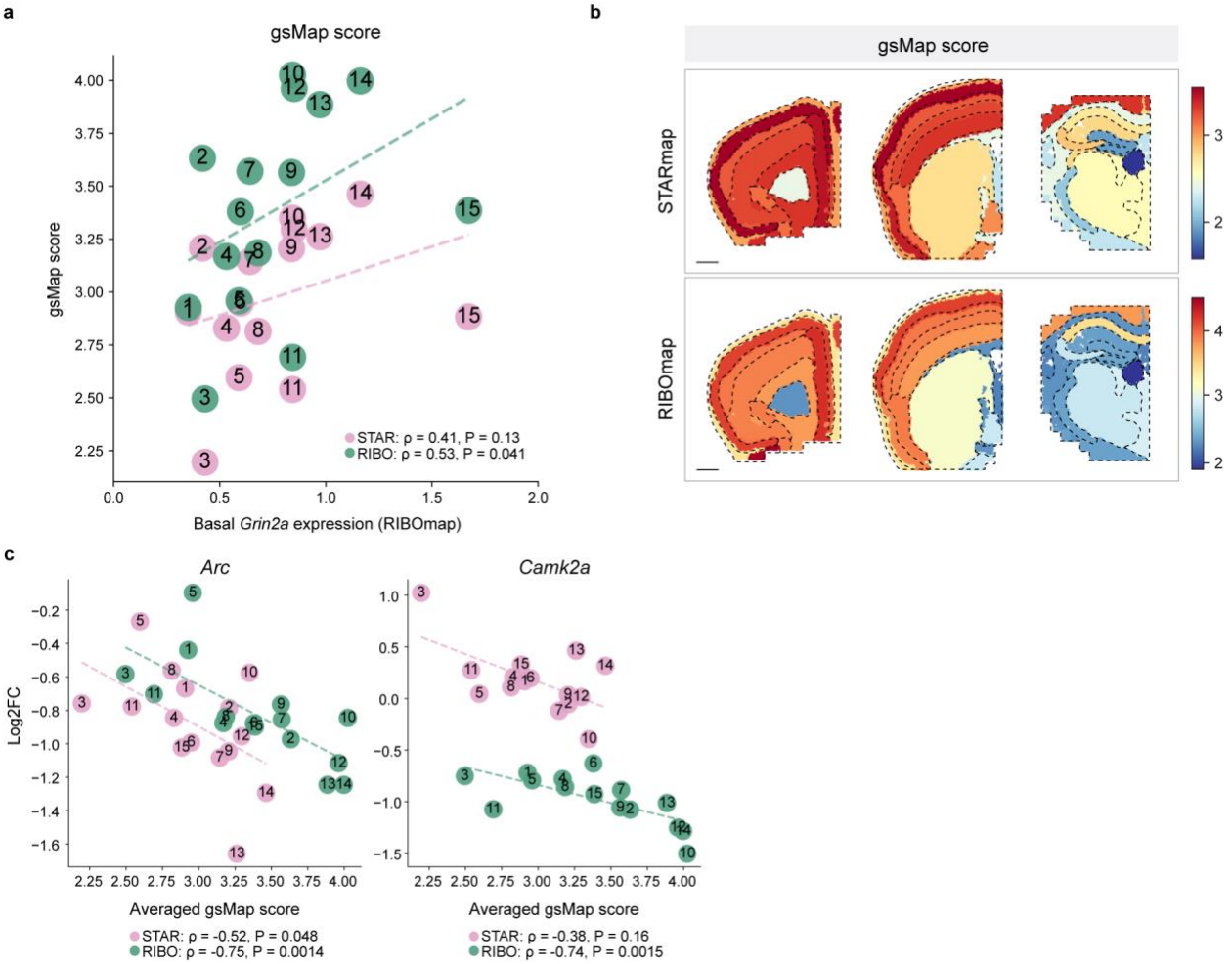


**Extended Data Fig. 7: Mapping human GWAS traits to STARmap/RIBOmap data with gsMap.**

**a**, Scatter plot showing the correlation between basal RIBOmap *Grin2a* expression level and gsMap score prediction across neuronal subtypes. **b**, Spatial heterogeneity of averaged gsMap score in STARmap (top) and RIBOmap (bottom) across tissue regions. Scale bar, 1mm. **c**, Relationship between the gsMap score and the RIBOmap log fold-change of example genes across neuronal subtypes.

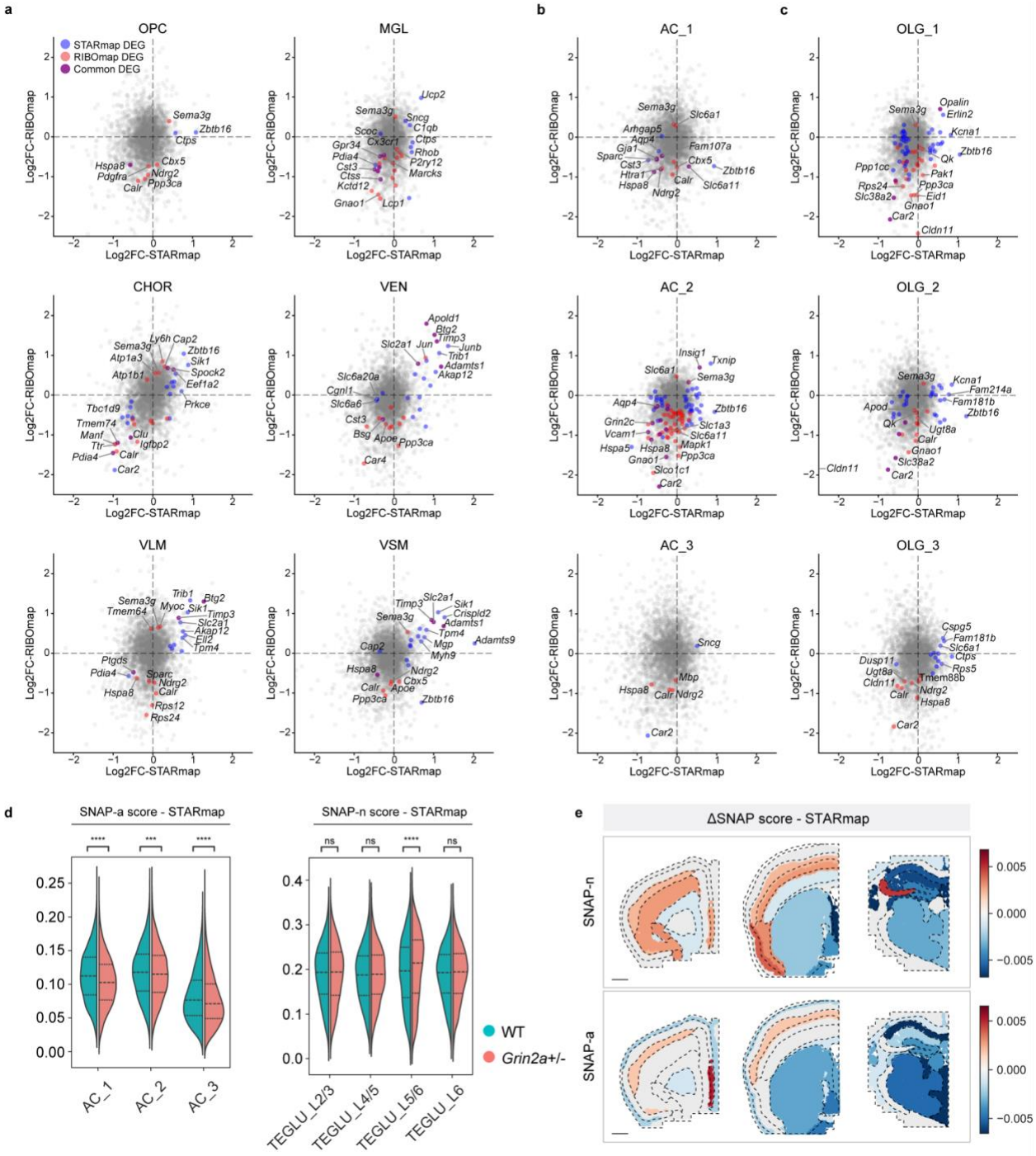


**Extended Data Fig. 8: Non-neuronal cell type DEG**

**a**, STARmap vs. RIBOmap log fold-change plot of 6 remaining non-neuron major cell types. **b-c**, STARmap vs. RIBOmap log fold-change plot of astrocyte (**b**) and oligodendrocyte (**c**) subtypes. **d**, Violin plots illustrating the difference between WT and *Grin2a*+/- in SNAP-a gene program scores in astrocyte subtypes (left) and in SNAP-n gene program scores in cortical TEGLU subtypes (right) in STARmap. P values were calculated using a two-sided independent t-test.

1094 ****P < 0.0001. **e**, Spatial visualizations of SNAP-n score difference in cortical neurons (top) and
1095 SNAP-a score difference in astrocytes (bottom) in STARmap. Scale bar, 1mm.

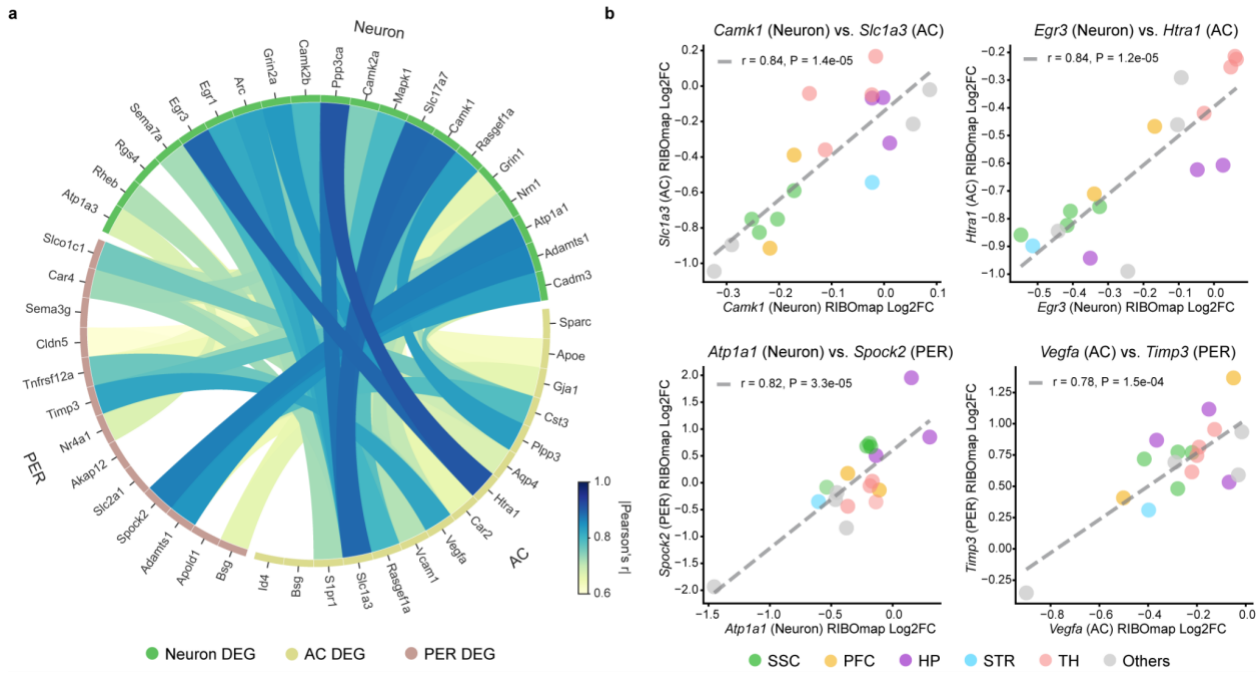


**Extended Data Fig. 9: NVU-associated cross-cell-type DEG correlation**

**a**, Chord diagram showing pairwise cross-cell-type NVU-associated DEG correlations of region-specific RIBOmap log fold-change in neuron, astrocyte, and pericyte. Chord color, absolute value of pairwise Pearson's correlation coefficient r. **b**, Relationship between RIBOmap log fold-changes of example cross-cell-type DEG pairs.